

Fundamental limits on the rate of bacterial cell division

³ Nathan M. Belliveau^{†, 1}, Griffin Chure^{†, 2}, Christina L. Hueschen³, Hernan G. Garcia⁴, Jane Kondev⁵, Daniel S. Fisher⁶, Julie A. Theriot^{1, 7, *}, Rob Phillips^{8, 9, *}

⁵ ¹Department of Biology, University of Washington, Seattle, WA, USA; ²Department of Applied Physics, California Institute of Technology, Pasadena, CA, USA; ³Department of Chemical Engineering, Stanford University, Stanford, CA, USA; ⁴Department of Molecular Cell Biology and Department of Physics, University of California Berkeley, Berkeley, CA, USA; ⁵Department of Physics, Brandeis University, Waltham, MA, USA; ⁶Department of Applied Physics, Stanford University, Stanford, CA, USA; ⁷Allen Institute for Cell Science, Seattle, WA, USA; ⁸Division of Biology and Biological Engineering, California Institute of Technology, Pasadena, CA, USA; ⁹Department of Physics, California Institute of Technology, Pasadena, CA, USA; *Co-corresponding authors. Address correspondence to phillips@pboc.caltech.edu and jtheriot@uw.edu; [†]These authors contributed equally to this work

14

¹⁵ **Abstract** Recent years have seen a deluge of experiments dissecting the relationship between bacterial growth rate, cell size, and protein content, quantifying the abundance of proteins across growth conditions with unprecedented resolution. However, we still lack a rigorous understanding of what sets the scale of these quantities and when protein abundances should (or should not) depend on growth rate. Here, we seek to quantitatively understand this relationship across a collection of *Escherichia coli* proteomic data sets covering \approx 4000 proteins and 36 growth rates. We estimate the basic requirements for steady-state growth by considering key processes in nutrient transport, energy generation, cell envelope biogenesis, and the central dogma. From these estimates, ribosome biogenesis emerges as a primary determinant of growth rate. We expand on this assessment by exploring a model of ribosomal regulation as a function of the nutrient supply, revealing a mechanism that ties cell size and growth rate to ribosomal content.

25

26 Introduction

27 The observed range of bacterial growth rates is enormously diverse. In natural environments, some microbial organisms may double only once per year (*Mikucki et al., 2009*) while in comfortable laboratory conditions, growth 28 can be rapid with several divisions per hour (*Schaechter et al., 1958*). This six order-of-magnitude difference in 29 time scales encompasses different microbial species and lifestyles, yet even for a single species such as *Escherichia* 30 *coli*, the growth rate can be modulated over a comparably large scale by tuning the type and amount of nutrients 31 in the growth medium. This remarkable flexibility in growth rate illustrates the intimate relationship between 32 environmental conditions and the rates at which cells convert nutrients into new cellular material – a relationship 33 that has remained a major topic of inquiry in bacterial physiology for over a century (*Jun et al., 2018*).

35 Jacques Monod once remarked that “the study of the growth of bacterial cultures does not constitute a specialized 36 subject or branch of research, it is the basic method of Microbiology.” Those words ring as true today as 37 they did when they were written 70 years ago (*Monod, 1949*) with the quantitative power of this “method” recently 38 undergoing renaissance. Many of the key questions addressed by the pioneering efforts in the middle of the last 39 century can be revisited by examining them through the lens of the increasingly refined molecular census that is 40 available for bacteria such as the microbial workhorse *E. coli*.

41 Several of the evergreen questions about bacterial growth and physiology that were originally raised by micro-

42 biologists in the middle of the 20th century can now be reframed in light of this newly available data. For example,
43 what biological processes are the primary determinants for how quickly bacterial cells can grow and reproduce?
44 How do cells modulate the absolute numbers and relative ratios of their molecular constituents as a function of
45 changes in growth rate or nutrient availability? In this paper, we begin by considering these two questions from
46 two distinct angles. First, as a result of an array of high-quality proteome-wide measurements of *E. coli* under
47 diverse growth conditions, we have a census that allows us to explore how the number of key molecular players
48 change as a function of growth rate. Here, we have assembled a singular data set using measurements collected
49 over the past decade via mass spectrometry (*Schmidt et al., 2016; Peebo et al., 2015; Valgepea et al., 2013*) or
50 ribosomal profiling (*Li et al., 2014*) of the composition of the *E. coli* proteome across 36 unique growth rates (see
51 Appendix Experimental Details Behind Proteomic Data for further discussion of the data). Second, by compiling
52 molecular turnover rate measurements for many of the fundamental processes associated with bacterial growth,
53 we make quantitative estimates of key cellular processes (schematized in *Figure 1*) to determine whether our current
54 understanding of the dynamics of these processes are sufficient to explain the magnitude of the observed
55 protein copy numbers across conditions. The census, combined with these estimates, provide a window into the
56 question of whether the rates of central processes such as energy generation or DNA synthesis are regulated
57 systematically as a function of cell growth rate by altering protein copy number.

58 Throughout our estimates, we consider an archetypal growth rate of $\approx 0.5 \text{ hr}^{-1}$ corresponding to a doubling
59 time of ≈ 5000 seconds, as the data sets examined here heavily sample this growth regime. While we formulate
60 point estimates for the protein abundances at this division time, we also consider how these values will vary
61 at other growth rates due to changes in cell size, surface area, and chromosome copy number (*Taheri-Araghi*
62 *et al., 2015*). Broadly, we find that the protein copy numbers appeared tuned for the task of cell doubling across
63 a continuum of growth rates for the majority of the processes estimated here. Thus, our understanding of the
64 kinetics of myriad biological processes is sufficient to quantitatively explain the observed abundances of these
65 proteins.

66 From these estimates, it emerges that translation, particularly the synthesis of ribosomal proteins, is a plausible
67 candidate that limits the rate of cell division. We reach this conclusion by considering that ribosome synthesis is
68 1) a rate limiting step for the *fastest* bacterial division, and 2) a major determinant of bacterial growth across
69 the nutrient conditions we have considered under steady state, exponential growth. This enables us to suggest
70 that the long-observed correlation between growth rate and cell size (*Schaechter et al., 1958; Si et al., 2017*)
71 can be simply attributed to the increased absolute number of ribosomes per cell under conditions supporting
72 extremely rapid growth. To better understand how the observed alterations in absolute protein abundances,
73 and in particular, changes in ribosome copy number, influence growth rate across different nutrient conditions
74 we consider a minimal model of cellular growth. Our conclusions from these analyses provide important insight
75 into how *E. coli* regulates growth across conditions of differing nutrient availability and identifies fundamental
76 constraints in bacterial growth more broadly.

117 Nutrient Transport

118 We begin by considering the critical transport processes diagrammed in *Figure 1(A)*. In order to build new cellular
119 mass, the molecular and elemental building blocks must be scavenged from the environment in different forms.
120 Carbon, for example, is acquired via the transport of carbohydrates and sugar alcohols with some carbon sources
121 receiving preferential treatment in their consumption (*Monod, 1947*). Phosphorus, sulfur, and nitrogen, on the
122 other hand, are harvested primarily in the forms of inorganic salts, namely phosphate, sulfate, and ammonia
123 (*Jun et al., 2018; Assentoft et al., 2016; Stasi et al., 2019; Antonenko et al., 1997; Rosenberg et al., 1977; Willsky*
124 *et al., 1973*). All of these compounds have different membrane permeabilities (*Phillips, 2018*) and most require
125 some energetic investment either via ATP hydrolysis or through the proton electrochemical gradient to bring the
126 material across the hydrophobic cell membrane.

127 The elemental composition of *E. coli* has received much quantitative attention over the past half century (*Neidhardt et al., 1991; Taymaz-Nikerel et al., 2010; Heldal et al., 1985; Bauer and Ziv, 1976*), providing us with a
128 starting point for estimating how many atoms of each element must be scavenged from the environment. A synthesis
129 of these studies presents an approximate dry mass composition of $\approx 50\%$ carbon (BNID: 100649, see *Box 1*),
130 $\approx 15\%$ nitrogen (BNID: 106666), $\approx 3\%$ phosphorus (BNID: 100653), and 1% sulfur (BNID: 100655) with remainder

78

Box 1. The Rules of Engagement for Order-Of-Magnitude Estimates

79

This work relies heavily on "back-of-the-envelope" estimates to understand the growth-rate dependent abundances of molecular complexes. This moniker arises from the limitation that any estimate should be able to fit on the back of a postage envelope. As such, we must draw a set of rules governing our precision and sources of key values.

80

The rule of "one, few, and ten". The philosophy behind order-of-magnitude estimates is to provide an estimate of the appropriate scale, not a prediction with many significant digits. We therefore define three different scales of precision in making estimates. The scale of "one" is reserved for values that range between 1 and 2. For example, If a particular process has been experimentally measured to transport 1.87 protons for a process to occur, we approximate this process to require 2 protons per event. The scale of "few" is reserved for values ranging between 3 and 7. For example, we will often use Avogadro's number to compute the number of molecules in a cell given a concentration and a volume. Rather than using Avogadro's number as 6.02214×10^{23} , we will approximate it as 5×10^{23} . Finally, the scale of "ten" is reserved for values which we know within an order of magnitude. If a particular protein complex is present at 883 copies per cell, we say that it is present in approximately 10^3 copies per cell. These different scales will be used to arrive at simple estimates that report the expected scale of the observed data. Therefore, the estimates presented here should not be viewed as hard-and-fast predictions of precise copy numbers, but as approximate lower (or upper) bounds for the number of complexes that may be needed to satisfy some cellular requirement.

81

Furthermore, we use equality symbols (=) sparingly and frequently defer to approximation (\approx) or scaling (\sim) symbols when reporting an estimate. When \approx is used, we are implicitly stating that we are confident in this estimate within a factor of a few. When a scaling symbol \sim is used, we are stating that we are confident in our estimate to within an order of magnitude.

82

The BioNumbers Database as a source for values. In making our estimates, we often require approximate values for key cellular properties, such as the elemental composition of the cell, the average dry mass, or approximate rates of synthesis. We rely heavily on the BioNumbers Database (bionumbers.hms.harvard.edu, *Milo et al. (2010)*) as a repository for such information. Every value we draw from this database has an associated BioNumbers ID number, abbreviated as BNID, and we provide this reference in grey-boxes in each figure.

83

Uncertainty in the data sets and the accuracy of an estimate. The data sets presented in this work are the products of careful experimentation with the aim to report, to the best of their ability, the absolute copy numbers of proteins in the cell. These data, collected over the span of a few years, come from different labs and use different internal standards, controls, and even techniques (discussed further in Appendix Experimental Details Behind Proteomic Data). As a result, there is notable disagreement in the measured copy numbers for some complexes across data sets. In assessing whether our estimates could explain the observed scales and growth-rate dependencies, we also considered the degree of variation between the different data sets. For example, say a particular estimate undercuts the observed data by an order of magnitude. If all data sets agree within a factor of a few of each other, we revisit our estimate and consider what we may have missed. However, if the data sets themselves disagree by an order of magnitude, we determine that our estimate is appropriate given the variation in the data.

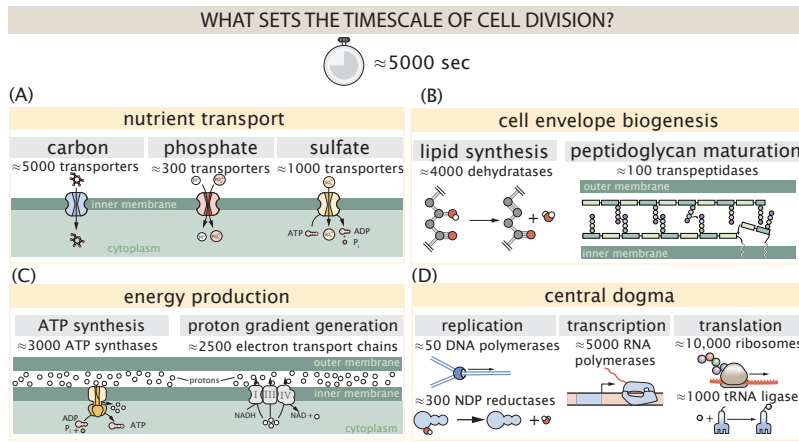


Figure 1. Transport and synthesis processes necessary for cell division. We consider an array of processes necessary for a cell to double its molecular components, broadly grouped into four classes. These categories are (A) nutrient transport across the cell membrane, (B) cell envelope biogenesis, (C) energy production (namely, ATP synthesis), and (D) processes associated with the central dogma. Numbers shown are the approximate number of complexes of each type observed at a growth rate of 0.5 hr^{-1} , or a cell doubling time of $\approx 5000 \text{ s}$.

132 being attributable to oxygen, hydrogen, and various transition metals. We use this stoichiometric breakdown to
 133 estimate the abundance and growth rate dependence of a variety of transporters responsible for carbon uptake,
 134 and provide more extensive investigation of the other critical elements – phosphorus, sulfur, and nitrogen – in the
 135 Appendix ??.

136 Using $\approx 0.3 \text{ pg}$ as the typical *E. coli* dry mass at a growth rate of $\approx 0.5 \text{ hr}^{-1}$ (BNID: 103904), coupled with an
 137 approximation that $\approx 50\%$ of this mass is carbon, we estimate that $\sim 10^{10}$ carbon atoms must be brought into
 138 the cell in order to double all of the carbon-containing molecules (Figure 2(A), top). Typical laboratory growth
 139 conditions provide carbon as a single class of sugar (such as glucose, galactose, or xylose) often transported cross
 140 the cell membrane by a transporter complex specific to that particular sugar. One such mechanism of transport
 141 is via the PTS system which is a highly modular system capable of transporting a diverse range of sugars with
 142 high specificity (Escalante *et al.*, 2012). The glucose-specific component of this system transports ≈ 200 glucose
 143 molecules (≈ 1200 carbon atoms) per second per transporter (BNID: 114686). Making the assumption that this
 144 is a typical sugar transport rate for the PTS system, coupled with the need to transport $\sim 10^{10}$ carbon atoms, we
 145 then expect on the order of ≈ 1000 transporters must be expressed per cell in order to bring in enough carbon
 146 atoms (Figure 2(A), top).

147 However, we find this estimate to be exceeded by several fold by experimental measurements (Figure 2(A),
 148 bottom), implying that the cell is capable of transporting more carbon atoms than strictly needed for biosynthesis.
 149 While we estimate ≈ 1000 transporters are needed with a 5000 second division time, we can abstract this
 150 calculation to consider any particular growth rate given knowledge of the cell density and volume as a function
 151 of growth rate and direct the reader to the Appendix Extending Estimates to a Continuum of Growth Rates for
 152 more information. This abstraction, shown as a grey line in Figure 2(A), reveals an excess of transporters even at
 153 faster growth rates. This contrasts with our observations for uptake of phosphorus and sulfur, which align well
 154 with our expectations across different growth conditions (Figure 2–Figure Supplement 1 and discussed further in
 155 Appendix ??).

156 It is important to note, however, that this estimate neglects any specifics of the regulation of the carbon trans-
 157 port system. Using the diverse array of growth conditions available in the data, we can explore how individual
 158 carbon transport systems depend on specific carbon availability. In Figure 2(B), we show the total number of
 159 carbohydrate transporters specific to different carbon sources. A striking observation, shown in the top-left plot
 160 of Figure 2(B), is the constancy in the expression of the glucose-specific transport systems, an observation that
 161 stands in contrast with other species of transporters. Additionally, we note that the total number of glucose-
 162 specific transporters is tightly distributed at $\approx 10^4$ per cell, the approximate number of transporters needed to
 163 sustain rapid growth of several divisions per hour. This illustrates that *E. coli* maintains a substantial number of

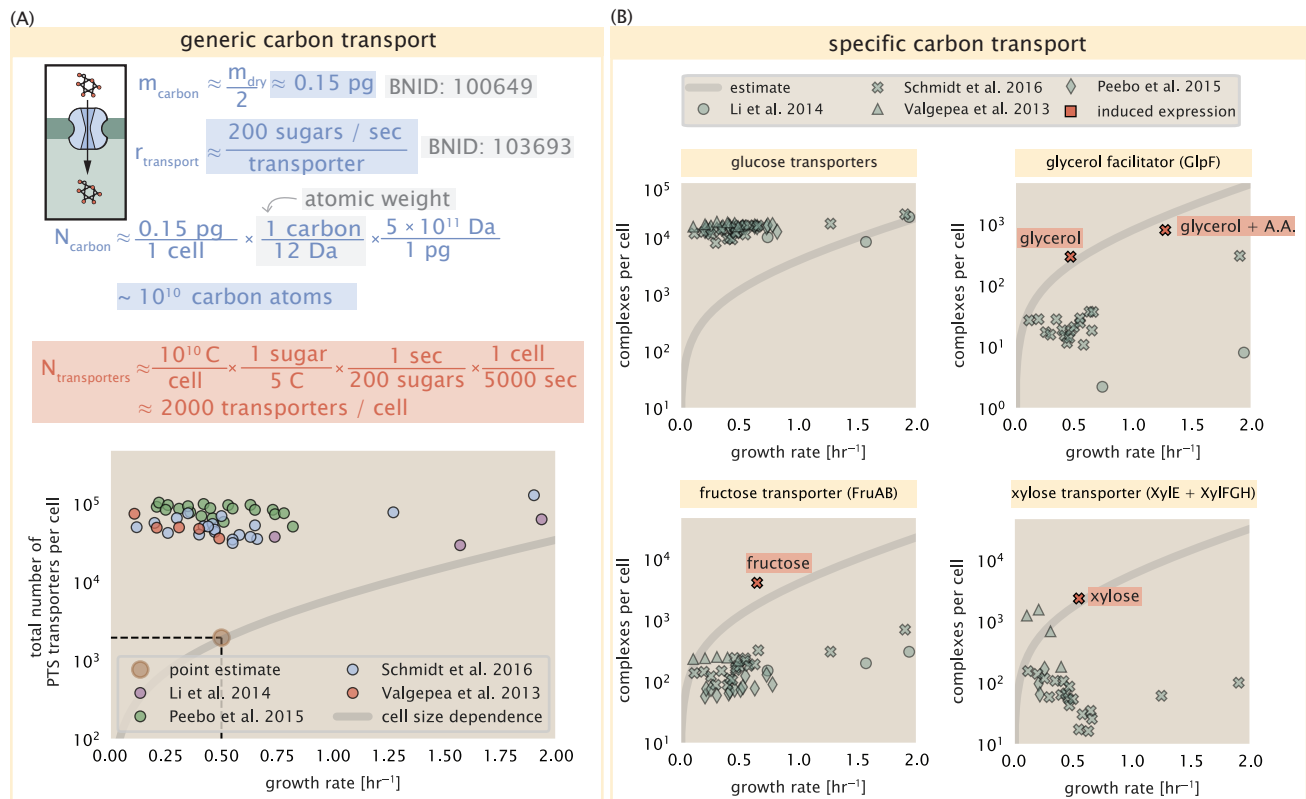


Figure 2. The abundance of carbon transport systems across growth rates. (A) A simple estimate for the minimum number of generic carbohydrate transport systems (top) assumes $\sim 10^{10}$ C are needed to complete division, each transported sugar contains ≈ 5 C, and each transporter conducts sugar molecules at a rate of ≈ 200 per second. Bottom plot shows the estimated number of transporters needed at a growth rate of ≈ 0.5 per hr (light-brown point and dashed lines). Colored points correspond to the mean number of complexes involved in carbohydrate import (complexes annotated with the Gene Ontology terms GO:0009401 and GO:0098704) for different growth conditions across different published datasets. (B) The abundance of various specific carbon transport systems plotted as a function of the population growth rate. The rates of substrate transport differ between these transporter species. To compute the continuum growth rate estimate (grey line), we used the following transport rates for each transporter species: 200 glucose- s^{-1} (BNID: 103693), 2000 glycerol- s^{-1} (**Lu et al., 2003**), 200 fructose- s^{-1} (assumed to be similar to PtsI, BNID: 103693), and 50 xylose- s^{-1} (assumed to be comparable to LacY, BNID: 103159). Red points and highlighted text indicate conditions in which the only source of carbon in the growth medium induces expression of the transport system. Grey lines in (A) and (B) represent the estimated number of transporters per cell at a continuum of growth rates.

Figure 2-Figure supplement 1. Estimates and observed abundances of phosphate and sulfate transporters.

164 complexes present for transporting glucose regardless of growth condition, which is known to be the preferential
165 carbon source (*Monod, 1947; Liu et al., 2005; Aidelberg et al., 2014*).

166 Many metabolic operons are regulated with dual-input logic gates that are only expressed when glucose con-
167 centrations are low and the concentration of other carbon sources are elevated (*Gama-Castro et al., 2016; Zhang*
168 *et al., 2014; Gama-Castro et al., 2016; Belliveau et al., 2018; Ireland et al., 2020*). Points colored in red in *Fig-*
169 *ure 2(B)* (labeled by red text-boxes) correspond to growth conditions in which the specific carbon source (glycerol,
170 xylose, or fructose) is present as the sole source of carbon. The grey lines in *Figure 2(B)* show the estimated
171 number of transporters needed at each growth rate to satisfy the cellular carbon requirement, adjusted for the
172 specific carbon source in terms of number of carbon atoms per molecule and the rate of transport for the par-
173 ticular transporter species. These plots show that, in the absence of the particular carbon source, expression of
174 the transporters is maintained on the order of $\sim 10^2$ per cell. The low but non-zero abundances may reflect the
175 specific regulatory logic involved, requiring that cells are able to transport some minimal amount of an alternative
176 carbon source in order to induce expression of these alternative carbon-source systems.

177 **Limits on Transporter Expression**

178 If acquisition of nutrients was a limiting process in cell division under the typical growth conditions explored here,
179 the growth rate could be theoretically increased simply by expressing more transporters, but is this feasible at
180 a physiological level? A way to approach this question is to compute the amount of space in the bacterial mem-
181 brane that could be occupied by nutrient transporters. Considering a rule-of-thumb for the surface area of *E.*
182 *coli* of about $5 \mu\text{m}^2$ (BNID: 101792), we expect an areal density for 1000 transporters to be approximately 200
183 transporters/ μm^2 . For a typical transporter occupying about 50 nm^2 , this amounts to about only $\approx 1\%$ of the
184 total inner membrane area (*Szenk et al., 2017*). Additionally, bacterial cell membranes typically have densities
185 of 10^5 proteins/ μm^2 (*Phillips, 2018*), implying that the cell could accommodate more membrane and this places
186 additional limitations on cell size and surface area that we will consider further in the coming sections.

187 **Cell Envelope Biogenesis**

188 In contrast to nutrient transporters, which support the synthesis of biomolecules throughout the cell and therefore
189 need to scale with the cell size, here we must consider the synthesis of components that will need to scale with the
190 surface area of the cell. *E. coli* is a rod-shaped bacterium with a remarkably robust length-to-width aspect ratio of
191 $\approx 4:1$ (*Harris and Theriot, 2018; Ojkic et al., 2019*). At modest growth rates, the total cell surface area is $\approx 5 \mu\text{m}^2$
192 (BNID: 101792). Assuming this surface area is approximately the same between the inner and outer membranes
193 of *E. coli*, and the fact that each membrane is itself a lipid bilayer, cells have a the total membrane surface area of
194 $\approx 20 \mu\text{m}^2$ (see Appendix Estimation of Cell Size and Surface Area for a description of the calculation of cell surface
195 area as a function of cell size). In this section, we will estimate the number of protein complexes needed to
196 produce this membrane surface area as well as the complexes involved in assembling the peptidoglycan scaffold
197 it encapsulates.

198 **Lipid Synthesis**

199 The dense packing of the membrane with proteins means that the cell membranes are not composed entirely
200 of lipid molecules, with only $\approx 40\%$ of the membrane area is occupied by lipids (BNID: 100078). Using a rule-of-
201 thumb of 0.5 nm^2 as the surface area of the typical lipid (BNID: 106993), we can estimate $\sim 2 \times 10^7$ lipids per cell,
202 which is in close agreement with experimental measurements (BNID: 100071, 102996).

203 The membranes of *E. coli* are composed of a variety of different lipids, each of which are unique in their struc-
204 tures and biosynthetic pathways (*Sohlenkamp and Geiger, 2016*). Recently, a combination of stochastic kinetic
205 modeling (*Ruppe and Fox, 2018*) and *in vitro* kinetic measurements (*Ranganathan et al., 2012; Yu et al., 2011*)
206 have revealed remarkably slow steps in the fatty acid synthesis pathways which may serve as the rate limiting
207 reactions for making new membrane phospholipids. One such step is the removal of hydroxyl groups from the
208 fatty-acid chain by ACP dehydratase that leads to the formation of carbon-carbon double bonds. This reaction,
209 catalyzed by proteins FabZ and FabA in *E. coli* (*Yu et al., 2011*), have been estimated to have kinetic turnover rates
210 of ≈ 1 dehydration per second per enzyme (*Ruppe and Fox, 2018*). Thus, given this rate and the need to synthe-
211 size $\approx 2 \times 10^7$ lipids over 5000 seconds, one can estimate that a typical cell requires ≈ 4000 ACP dehydratases.

212 This is in reasonable agreement with the experimentally observed copy numbers of FabZ and FabA (*Figure 3(A)*).
213 Furthermore, we can extend this estimate to account for the change in membrane surface area as a function of
214 the growth rate (grey line in *Figure 3(A)*), which captures the observed growth rate dependent expression of these
215 two enzymes.

216 Peptidoglycan Synthesis

217 Bacterial cells demonstrate exquisite control over their cell shape. This is primarily due to the cell wall, a stiff, sev-
218 eral nanometer thick meshwork of polymerized discaccharides. The formation of the peptidoglycan is an intricate
219 process involving many macromolecular players (*Shi et al., 2018; Morgenstein et al., 2015*), whose coordinated
220 action maintains cell shape and integrity even in the face of large-scale perturbations (*Harris and Theriot, 2018;*
221 *Shi et al., 2018*). The peptidoglycan alone comprises $\approx 3\%$ of the cellular dry mass (BNID: 1019360, making it
222 the most massive molecule in *E. coli*). The polymerized unit of the peptidoglycan is a N-acetylglucosamine and
223 N-acetylmuramic acid disaccharide, of which the former is functionalized with a short pentapeptide. With a mass
224 of ≈ 1000 Da, this unit, which we refer to as a murein monomer, it is polymerized to form long strands in the
225 periplasm which are then attached to each other via their peptide linkers. Together, these quantities provide an
226 estimate of $\approx 5 \times 10^6$ murein monomers per cell.

227 The crosslinking of the pentapeptides between adjacent glycan strands is responsible for maintaining the struc-
228 tural integrity of the cell wall and, in principle, each murein monomer can be involved in such a crosslink. In some
229 microbes, such as in gram-positive bacterium *Staphylococcus aureus*, the extent of crosslinking can be large with
230 $> 90\%$ of pentapeptides forming a connection between glycan strands. In *E. coli*, however, a much smaller propor-
231 tion ($\approx 20\%$) of the peptides are crosslinked, resulting in a weaker and more porous cell wall (*Vollmer et al. (2008);*
232 *Rogers et al. (1980)*). The formation of these crosslinks occurs primarily during the polymerization of the murein
233 monomers and is facilitated by a family of enzymes called transpeptidases. The four primary transpeptidases of
234 *E. coli* have only recently been quantitatively characterized *in vivo* via liquid chromatography mass spectrometry
235 which revealed a notably slow kinetic turnover rate of ≈ 2 crosslinking reactions formed per second per enzyme
236 (*Catherwood et al., 2020*).

237 Assembling these quantities permits us to make an estimate that on the order of ≈ 100 transpeptidases per cell
238 are needed for complete maturation of the peptidoglycan, given a division time of ≈ 5000 seconds; a value that is
239 comparable to experimental observations (*Figure 3(B)*). Expanding this estimate to account for the changing mass
240 of the peptidoglycan as a function of growth rate (grey line in *Figure 3(B)*) also qualitatively captures the observed
241 dependence in the data, though systematic disagreements between the different data sets makes the comparison
242 more difficult.

243 Limits on Cell Wall Biogenesis

244 While the processes we have considered represent only a small portion of proteins devoted to cell envelope bio-
245 genesis, we find it unlikely that they limit cellular growth in general. The relative amount of mass required for lipid
246 and peptidoglycan components decrease at faster growth rates due to a decrease in their surface area to volume
247 (S/V) ratio (*Ojicic et al., 2019*). Furthermore, despite the slow catalytic rate of FabZ and FabA in lipid synthesis, exper-
248 imental data and recent computational modeling has shown that the rate of fatty-acid synthesis can be drastically
249 increased by increasing the concentration of FabZ (*Yu et al., 2011; Ruppe and Fox, 2018*). With a proteome size
250 of $\approx 3 \times 10^6$ proteins, a hypothetical 10-fold increase in expression from 4000 to 40,000 ACP dehydratases would
251 result in a paltry $\approx 1\%$ increase in the size of the proteome. In the context of peptidoglycan synthesis, we note
252 that our estimate considers only the transpeptidase enzymes that are involved lateral and longitudinal elongation
253 of the peptidoglycan. This neglects the presence of other transpeptidases that are present in the periplasm and
254 also involved in remodeling and maturation of the peptidoglycan. It is therefore possible that if this was setting
255 the speed limit for cell division, the simple expression of more transpeptidases may be sufficient to maintain the
256 structural integrity of the cell wall.

257 Energy Production

258 Cells consume and generate energy predominantly in the form of nucleoside triphosphates (NTPs) in order to
259 grow. The high-energy phosphodiester bonds of (primarily) ATP power a variety of cellular processes that drive

CELL ENVELOPE BIOSYNTHESIS

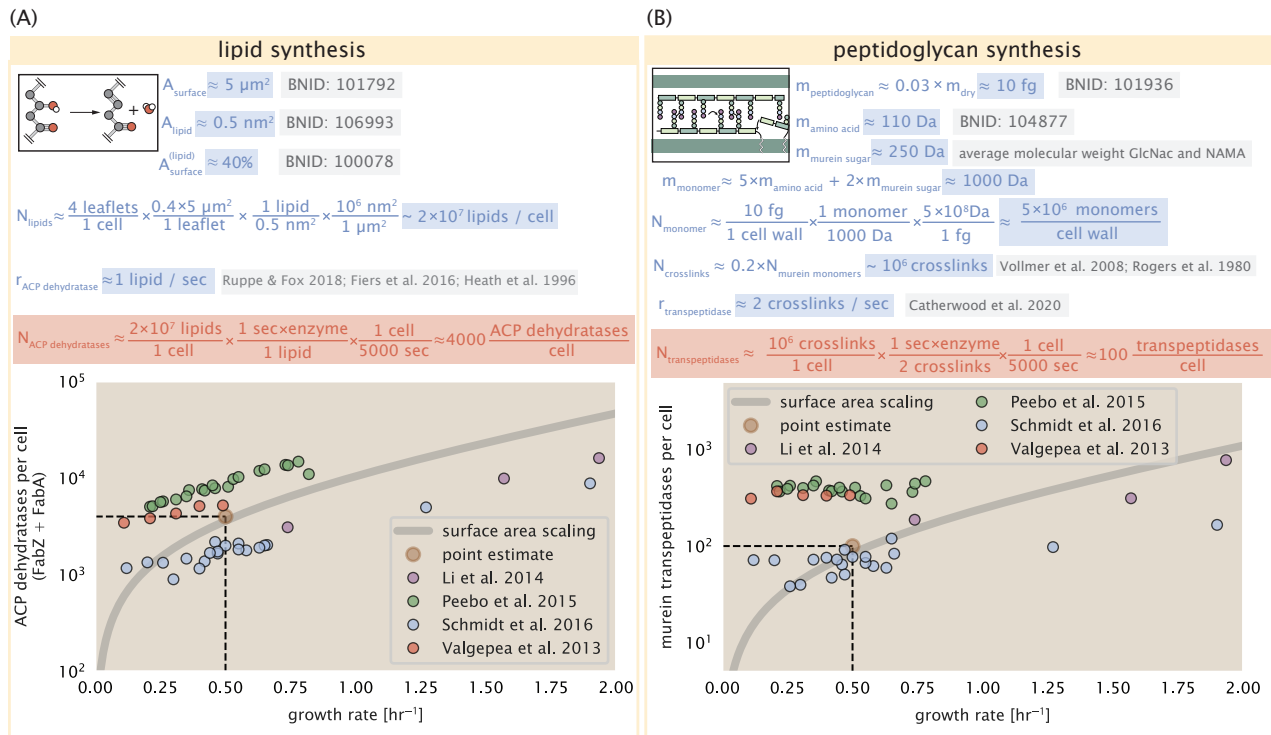


Figure 3. (A) Top panel shows an estimation for the number of ACP dehydratases necessary to form functional phospholipids, which is assumed to be a rate-limiting step on lipid synthesis. The rate of ACP dehydratases was inferred from experimental measurements via a stochastic kinetic model described in [Ruppe and Fox \(2018\)](#). Bottom panel shows the experimentally observed complex copy numbers using the stoichiometries $[\text{FabA}]_2$ and $[\text{FabZ}]_2$. (B) An estimate for the number of peptidoglycan transpeptidases needed to complete maturation of the peptidoglycan. The mass of the murein monomer was estimated by approximating each amino acid in the pentapeptide chain as having a mass of 110 Da and each sugar in the disaccharide having a mass of 250 Da. The *in vivo* rate of transpeptidation in *E. coli* was taken from recent analysis by [Catherwood et al. \(2020\)](#). The bottom panel shows experimental measurements of the transpeptidase complexes in *E. coli* following the stoichiometries $[\text{MrcA}]_2$, $[\text{MrcB}]_2$, $[\text{MrdA}]_1$, and $[\text{MrdB}]_1$. Grey curves in each plot show the estimated number of complexes needed to satisfy the synthesis requirements scaled by the surface area as a function of growth rate.

260 biological systems away from thermodynamic equilibrium. We next turn to the synthesis of ATP as a potential
261 process that may limit growth, which also requires us to consider the maintenance of the electrochemical proton
262 gradient which powers it.

263 **ATP Synthesis**

264 Hydrolysis of the terminal phosphodiester bond of ATP into ADP (or alternatively GTP and GDP) and an inorganic
265 phosphate provides the thermodynamic driving force in a wide array of biochemical reactions. One such reaction
266 is the formation of peptide bonds during translation, which requires ≈ 2 ATPs for the charging of an amino acid
267 to the tRNA and ≈ 2 GTP for the formation of each peptide bond. Assuming the ATP costs associated with error
268 correction and post-translational modifications of proteins are negligible, we can make the approximation that
269 each peptide bond has a net cost of ≈ 4 ATP (BNID: 101442, *Milo et al. (2010)*). Formation of GTP from ATP is
270 achieved via the action of nucleoside diphosphate kinase, which catalyzes this reaction without an energy invest-
271 ment (*Lascu and Gonin, 2000*) and therefore consider all NTP requirements of the cell to be functionally equivalent
272 to being exclusively ATP. In total, the energetic costs of peptide bond formation consume $\approx 80\%$ of the cells ATP
273 budget (BNID: 107782; 106158; 101637; 111918, *Lynch and Marinov (2015); Stouthamer (1973)*). The pool of ATP
274 is produced by the F₁-F₀ ATP synthase – a membrane-bound rotary motor which under ideal conditions can yield
275 ≈ 300 ATP per second (BNID: 114701; *Weber and Senior (2003)*).

276 To estimate the total number of ATP equivalents consumed during a cell cycle, we will make the approximation
277 that there are $\approx 3 \times 10^6$ proteins per cell with an average protein length of ≈ 300 peptide bonds (BNID: 115702;
278 108986; 104877). Taking these values together, coupled with an estimate of ≈ 4 ATP equivalents per peptide bond,
279 we find that the typical *E. coli* cell consumes $\sim 5 \times 10^9$ ATP per cell cycle on protein synthesis alone. Assuming that
280 each ATP synthases operates at its maximal speed (300 ATP per second per synthase), ≈ 3000 ATP synthases
281 are needed to keep up with the energy demands of the cell. This estimate is comparable with the experimental
282 observations, shown in *Figure 4* (A). We note that this estimate assumes all ATP is synthesized via ATP synthase
283 and neglects synthesis via fermentative metabolism. This assumption may explain why at the fastest growth rates
284 (≈ 2 hr⁻¹), our continuum estimate predicts more synthase than is experimentally observed (gray line in *Figure 4*).
285 At rapid growth rates, *E. coli* enters a type of overflow metabolism where fermentative metabolism becomes
286 pronounced (*Szenk et al., 2017*).

287 **Generating the Proton Electrochemical Gradient**

288 In order to produce ATP, the F₁-F₀ ATP synthase itself must consume energy. Rather than burning through its own
289 product (and violating thermodynamics), this intricate macromolecular machine has evolved to exploit the elec-
290 trochemical potential established across the inner membrane through cellular respiration. This electrochemical
291 gradient is manifest by the pumping of protons into the intermembrane space via the electron transport chains
292 as they reduce NADH. In *E. coli*, this potential difference is ≈ -200 mV (BNID: 102120). A simple estimate of the
293 inner membrane as a capacitor with a working voltage of -200 mV reveals that $\approx 2 \times 10^4$ protons must be present
294 in the intermembrane space. However, each rotation of an ATP synthase shuttles ≈ 4 protons into the cytosol
295 (BNID: 103390). With a few thousand ATP synthases producing ATP at their maximal rate, the potential difference
296 would be rapidly abolished in a few milliseconds if it were not being actively maintained.

297 The electrochemistry of the electron transport complexes of *E. coli* have been the subject of intense biochemical
298 and biophysical study (*Ingledew and Poole, 1984; Khademian and Imlay, 2017; Cox et al., 1970; Henkel et al., 2014*).
299 A recent work (*Szenk et al., 2017*) examined the respiratory capacity of the *E. coli* electron transport complexes
300 using structural and biochemical data, revealing that each electron transport chain rapidly pumps protons into
301 the intermembrane space at a rate of ≈ 1500 protons per second (BIND: 114704; 114687). Using our estimate
302 of the number of ATP synthases required per cell [*Figure 4(A)*], coupled with these recent measurements, we
303 estimate that ≈ 3000 electron transport complexes would be necessary to facilitate the $\sim 5 \times 10^6$ protons per
304 second diet of the cellular ATP synthases. This estimate is in agreement with the number of complexes identified
305 in the proteomic datasets (plot in *Figure 4(B)*). This suggests that every ATP synthase must be accompanied by \approx
306 1 functional electron transport chain.

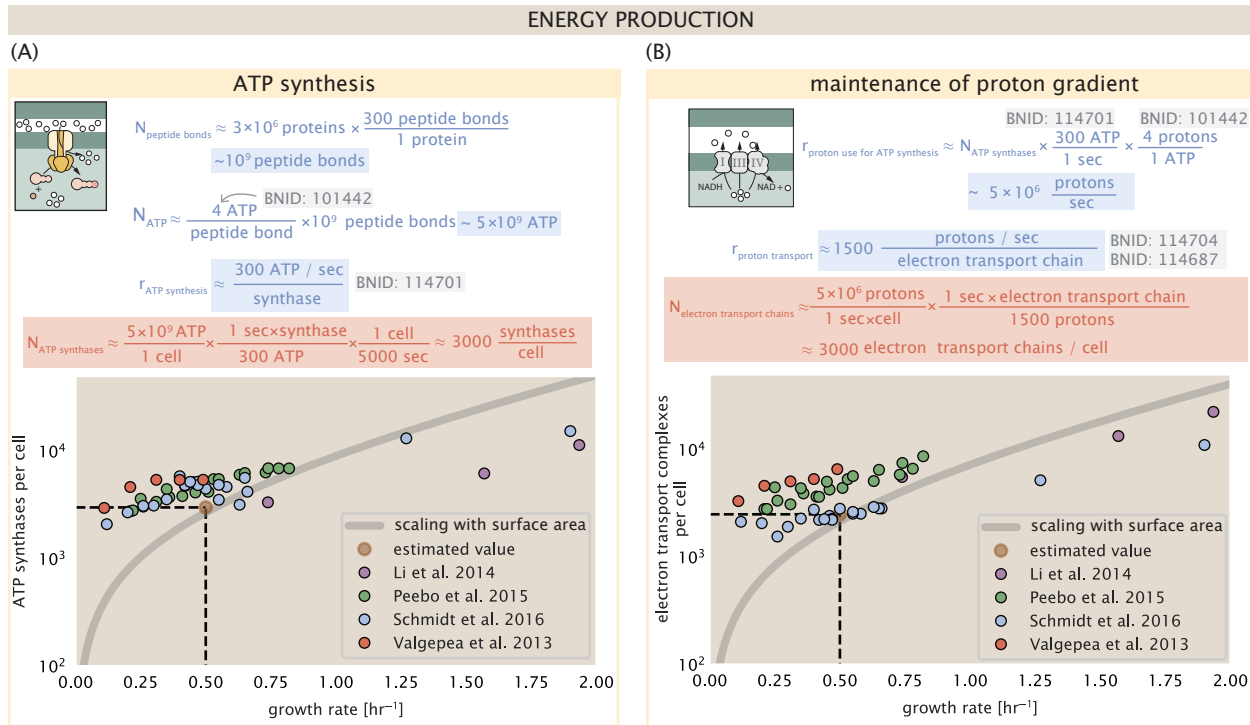


Figure 4. The abundance of F₁-F₀ ATP synthases and electron transport chain complexes as a function of growth rate.

(A) Estimate of the number of F₁-F₀ ATP synthase complexes needed to accommodate peptide bond formation and other NTP dependent processes. Points in plot correspond to the mean number of complete F₁-F₀ ATP synthase complexes that can be formed given proteomic measurements and the subunit stoichiometry [AtpE]₁₀[AtpF]₂[AtpB][AtpC][AtpH][AtpA]₃[AtpG][AtpD]₃. (B) Estimate of the number of electron transport chain complexes needed to maintain a membrane potential of -200 mV given estimate of number of F₁-F₀ ATP synthases from (A). Points in plot correspond to the average number of complexes identified as being involved in aerobic respiration by the Gene Ontology identifier GO:0019646 that could be formed given proteomic observations. These complexes include cytochromes *bd1* ([CydA][CydB][CydX][CydH]), *bdII* ([AppC][AppB]), *bo₃*,([CyoD][CyoA][CyoB][CyoC]) and NADH:quinone oxioreductase I ([NuoA][NuoH][NuoJ][NuoK][NuoL][NuoM][NuoN][NuoB][NuoC][NuoE][NuoF][NuoG][NuoI]) and II ([Ndh]). Grey lines in both (A) and (B) correspond to the estimate procedure described, but applied to a continuum of growth rates. We direct the reader to the Supporting Information for a more thorough description of this approach.

307 Limits on Biosynthesis in a Crowded Membrane

308 Our estimates thus far have focused on biochemistry at the periphery of the cell and have generally been con-
309 cordant with the abundances predicted by our estimates. However, as surface area and volume do not scale
310 identically, it is necessary to consider the physical limits for transport and energy production given the S/V ratio,
311 which as we've noted will decrease at faster growth rates.

312 In our estimate of ATP production above we found that a cell demands about 5×10^9 ATP per cell cycle or 10^6
313 ATP/s. With a cell volume of roughly 1 fL (BNID: 100004), this corresponds to about 2×10^{10} ATP per fL of cell
314 volume, in line with previous estimates (*Stouthamer and Bettenhausen, 1977; Szenk et al., 2017*). In *Figure 5* (A)
315 we plot this ATP demand as a function of the S/V ratio in green, where we have considered a range of cell shapes
316 from spherical to rod-shaped with an aspect ratio (length/width) equal to 4. In order to consider the maximum
317 ATP that could be produced, we consider the amount of ATP that can be generated by a membrane filled with ATP
318 synthase and electron transport complexes, which provides a maximal production of about 3 ATP / (nm²·s) (*Szenk*
319 *et al., 2017*). This is shown in blue in *Figure 5*(A), which shows that at least for the growth rates observed (right
320 column in plot), the energy demand is roughly an order of magnitude less. Interestingly, *Szenk et al. (2017)* also
321 found that ATP production by respiration is less efficient than by fermentation per membrane area occupied due
322 to the additional proteins of the electron transport chain. This suggests that, even under anaerobic growth, there
323 will be sufficient membrane space for ATP production.

324 The analysis highlights the diminishing capacity to provide resources as the cell increases in size. However,
325 the maximum energy production in *Figure 5*(A) does represents a somewhat unachievable limit since the inner
326 membrane must also include other proteins including those required for lipid and membrane synthesis. To bet-
327 ter understand the overall proteomic makeup of the inner membrane, we therefore used Gene Ontology (GO)
328 annotations (*Ashburner et al., 2000; The Gene Ontology Consortium, 2018*) to identify all proteins embedded
329 or peripheral to the inner membrane (GO term: 0005886). Those associated but not membrane-bound include
330 proteins like MreB and FtsZ and must nonetheless be considered as a vital component occupying space on the
331 membrane. In *Figure 5*(B), we find that the total protein mass per μm^2 is nearly constant across growth rates. In-
332 terestingly, when we consider the distribution of proteins grouped by their Clusters of Orthologous Groups (COG)
333 (*Tatusov et al., 2000*), the relative abundance for those in metabolism (including ATP synthesis via respiration) is
334 also relatively constant across growth rates, suggesting that no one process (energy production, nutrient uptake,
335 etc.) is particularly dominating even at fast growth rates *Figure 5*(C).

336 **Processes of the Central Dogma**

337 Up to this point, we have considered a variety of transport and biosynthetic processes that are critical to acquiring
338 and generating new cell mass. While there are of course many other metabolic processes we could consider, we
339 now turn our focus to some of the most central processes which *must* be undertaken irrespective of the growth
340 conditions – those of the central dogma.

341 **DNA Replication**

342 Most bacteria (including *E. coli*) harbor a single, circular chromosome and can have extra-chromosomal plasmids
343 up to ~ 100 kbp in length. While we consider the starting material dNTPs in *Figure 6–Figure Supplement 1* and
344 discussed further in Appendix ??, here we focus our quantitative thinking on the chromosome of *E. coli* which
345 harbors ≈ 5000 genes and $\approx 5 \times 10^6$ base pairs.

346 To successfully divide and produce viable progeny, this chromosome must be faithfully replicated and segre-
347 gated into each nascent cell. Replication is initiated at a single region of the chromosome termed the *oriC* locus
348 at which a pair of replisomes, each consisting of two DNA polymerase III, begin their high-fidelity replication of
349 the genome in opposite directions (*Fijalkowska et al., 2012*). *In vitro* measurements have shown that DNA Poly-
350 merase III copies DNA at a rate of ≈ 600 nucleotides per second (BNID: 104120). Therefore, to replicate a single
351 chromosome, two replisomes moving at their maximal rate would copy the entire genome in ≈ 4000 s. Thus, with
352 a division time of 5000 s, there is sufficient time for a pair of replisomes complexes to replicate the entire genome.

353 In rapidly growing cultures, bacteria like *E. coli* can initiate as many as 10 - 12 replication forks at a given time
354 (*Bremer and Dennis, 2008; Si et al., 2017*), we expect only a few DNA polymerases (≈ 10) are needed. However,

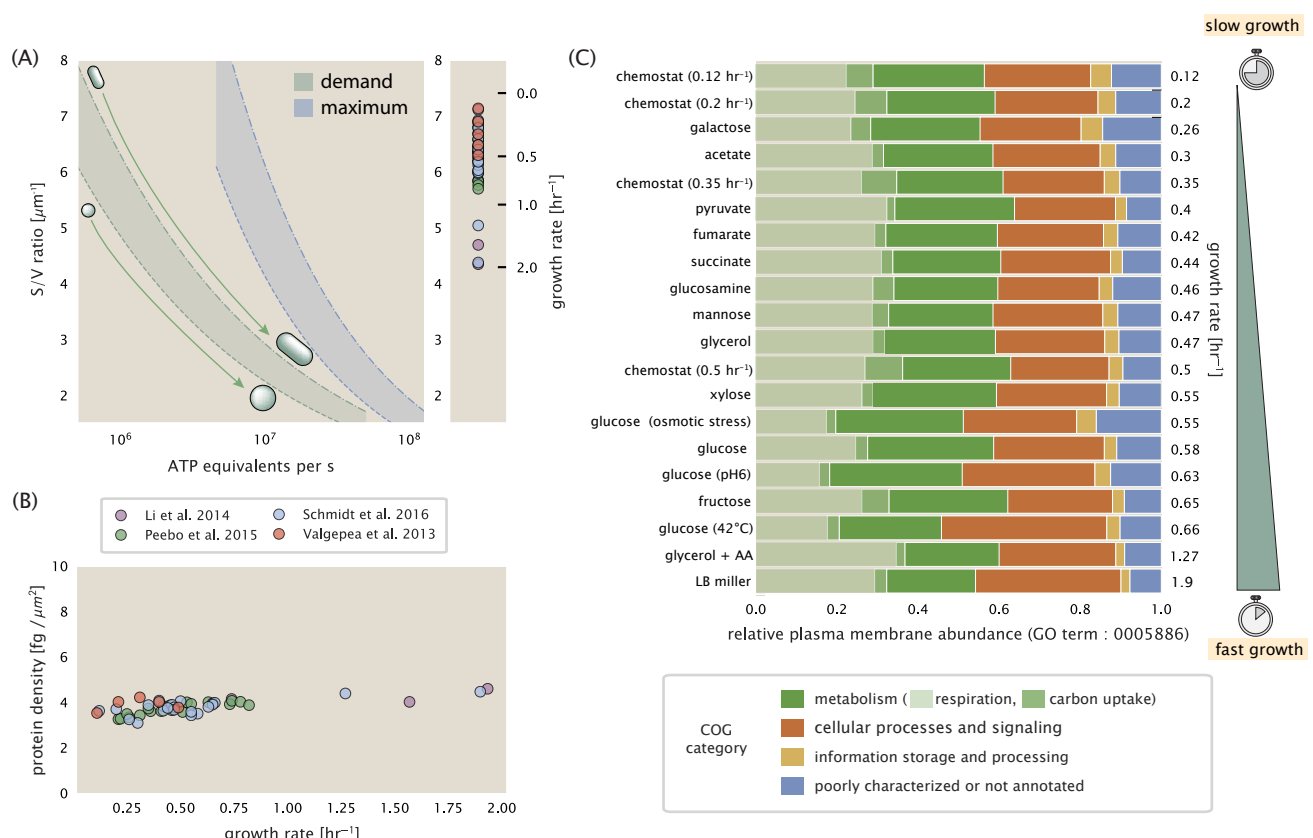


Figure 5. Influence of cell size and S/V ratio on ATP production and inner membrane composition. (A) Scaling of ATP demand and maximum ATP production as a function of S/V ratio. Cell volumes of 0.5 fL to 50 fL were considered, with the dashed (—) line corresponding to a sphere and the dash-dot line (---) reflecting a rod-shaped bacterium like *E. coli* with a typical aspect ratio (length / width) of 4 (Shi et al., 2018). Approximately 50% of the bacterial inner membrane is assumed to be protein, with the remainder lipid. The right plot shows the measured growth rates, and their estimated S/V ratio using growth rate dependent size measurements from Si et al. (2017) (See Appendix Estimation of Cell Size and Surface Area on calculation). (B) Total protein mass per μm^2 calculated for proteins with inner membrane annotation (GO term: 0005886). (C) Relative protein abundances by mass based on COG annotation. Metabolic proteins are further separated into respiration (F_1 - F_0 ATP synthase, NADH dehydrogenase I, succinate:quinone oxidoreductase, cytochrome bo_3 ubiquinol oxidase, cytochrome bd-ubiquinol oxidase) and carbohydrate transport (GO term: GO:0008643). Note that the elongation factor EF-Tu can also associate with the inner membrane, but was excluded in this analysis due to its high relative abundance (roughly identical to the summed protein shown in part (B)).

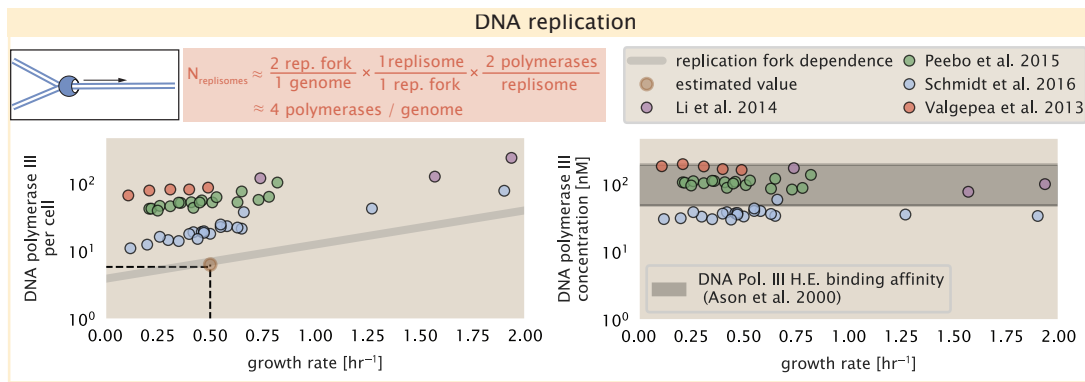


Figure 6. Complex abundance estimates for dNTP synthesis and DNA replication. An estimate for the minimum number of DNA polymerase holoenzyme complexes needed to facilitate replication of a single genome. Points in the left-hand plot correspond to the total number of DNA polymerase III holoenzyme complexes ($[\text{DnaE}]_3[\text{DnaQ}]_3[\text{HolE}]_3[\text{DnaX}]_5[\text{HolB}][\text{HolA}][\text{DnaN}]_4[\text{HolC}]_4[\text{Hold}]_4$) per cell. Right-hand plot shows the effective concentration of DNA polymerase III holoenzyme (See Appendix Estimation of Cell Size and Surface Area for calculation of cell size). Grey lines in left-hand panel show the estimated number of complexes needed as a function of growth, the details of which are described in the Supplemental Information.

Figure 6-Figure supplement 1. Estimate and observations of the abundance of ribonucleotide reductase, a key component in dNTP synthesis.

as shown in **Figure 6** DNA polymerase III is nearly an order of magnitude more abundant. This discrepancy can be understood by considering its binding constant to DNA. *In vitro* characterization has quantified the K_D of DNA polymerase III holoenzyme to single-stranded and double-stranded DNA to be 50 and 200 nM, respectively (Ason et al., 2000). The right-hand plot in **Figure 6** shows that the concentration of DNA polymerase III across all data sets is within this range. Thus, its copy number appears to vary such that its concentration is approximately equal to the dissociation constant to the DNA. While the processes regulating the initiation of DNA replication are complex and involve more than just the holoenzyme, these data indicate that the kinetics of replication rather than the explicit copy number of the DNA polymerase III holoenzyme is the more relevant feature of DNA replication to consider. In light of this, the data in **Figure 6** suggests that for bacteria like *E. coli*, DNA replication does not represent a rate-limiting step in cell division. However, it is worth noting that for bacterium like *C. crescentus* whose chromosomal replication is initiated only once per cell cycle (Jensen et al., 2001), the time to double their chromosome indeed represents an upper limit to their growth rate.

RNA Synthesis

We now turn our attention to the next stage of the central dogma – the transcription of DNA to form RNA. We consider three major groupings of RNA, namely the RNA associated with ribosomes (rRNA), the RNA encoding the amino-acid sequence of proteins (mRNA), and the RNA which links codon sequence to amino-acid identity during translation (tRNA).

rRNA serves as the catalytic and structural component of the ribosome, comprising approximately 2/3 of the total ribosomal mass, and is decorated with ≈ 50 ribosomal proteins. Each ribosome contains three rRNA molecules of lengths 120, 1542, and 2904 nucleotides (BNID: 108093), meaning each ribosome contains ≈ 4500 nucleotides overall. *In vivo* measurements of the kinetics of rRNA transcription have revealed that RNA polymerases are loaded onto the promoter of an rRNA gene at a rate of ≈ 1 per second (BNID: 111997, 102362). If RNA polymerases are constantly loaded at this rate, then we can assume that ≈ 1 functional rRNA unit is synthesized per second per rRNA operon. While *E. coli* possesses 7 of these operons per chromosome, the fact that chromosome replication can be parallelized means that the average dosage of rRNA genes can be substantially higher (up to ≈ 70 copies) at fast growth rates. At a growth rate of $\approx 0.5 \text{ hr}^{-1}$, however, the average cell has ≈ 1 copy of its chromosome and therefore approximately ≈ 7 copies of the rRNA operons, therefore producing ≈ 7 rRNA units per second. With a 5000 second division time, this means the cell is able to generate around 3×10^4 functional rRNA units, comparable within an order of magnitude to the number of ribosomes per cell.

384 How many RNA polymerases are then needed to constantly transcribe the required rRNA? If one polymerase is
385 loaded per second, and the transcription rate is \approx 40 nucleotides per second (BNID: 101094), then the typical
386 spacing between polymerases will be \approx 40 nucleotides. However, we must note that the polymerase itself has a
387 footprint of \approx 40 nucleotides (BNID: 107873), meaning that one could expect to find one RNA polymerase per 80
388 nucleotide stretch of an rRNA gene. With a total length of \approx 4500 nucleotides per operon and 7 operons per cell,
389 the number of RNA polymerases transcribing rRNA at any given time is then \approx 500 per cell.

390 As outlined in *Figure 7*, and discussed further the Appendix ??, synthesis of mRNA and tRNA together require
391 on the order of \approx 400 RNAP. Thus, in total, one would expect the typical cell to require \approx 1000 RNAP to satisfy
392 its transcriptional demands. As is revealed in *Figure 7(B)*, this estimate is about an order of magnitude below the
393 observed number of RNA polymerase complexes per cell (\approx 5000 - 7000). The difference between the estimated
394 number of RNA polymerase needed for transcription and these observations, however, are consistent with recent
395 literature revealing that \approx 80 % of RNA polymerases in *E. coli* are not transcriptionally active (Patrick et al., 2015).

396 Our estimates also neglect other mechanistic features of transcription and transcriptional initiation more
397 broadly. For example, we acknowledge that some fraction of the RNAP pool is nonspecifically bound to DNA
398 during its search for promoters from which to begin transcription. Furthermore, we ignore the obstacles that RNA
399 polymerase and DNA polymerase present to each other as they move along the DNA (Finkelstein and Greene,
400 2013). Finally, we neglect the fact that RNA polymerase also require σ -factors for promoter recognition and tran-
401 scription initiation (Browning and Busby, 2016).

402 While they are the machinery for transcription, RNA polymerase is not sufficient to initiate transcription. Pro-
403 moter recognition and initiation of transcription is dependent on the presence of σ -factors, protein cofactors
404 which bind directly to the polymerase (Browning and Busby, 2016). In *Figure 7–Figure Supplement 1*, we show
405 that the predicted RNA polymerase copy number indeed is more comparable with the abundance of σ -70 (RpoD),
406 the primary sigma factor in *E. coli*. There therefore remains more to be investigated as to what sets the observed
407 abundance of RNA polymerase in these proteomic data sets. However, we conclude that our the observed excess
408 in abundance for RNA polymerase abundances are generally in excess of what appears to be needed for growth,
409 suggesting that the abundance of RNA polymerase itself is not particularly limiting.

410 Protein Synthesis

411 The last process of the central dogma – the translation of RNA into protein – is the final subject in our dialogue
412 between back-of-the-envelope estimates and comparison with proteomic data. Here we consider the number of
413 ribosomes needed to replicate the cellular proteome. While the rate at which ribosomes translates is well known
414 to have a growth rate dependence (Dai et al., 2018), here we make the approximation that translation occurs at
415 a rate of \approx 15 amino acids per second per ribosome (BNID: 100233). Under this approximation and assuming a
416 division time of 5000 seconds, we can easily arrive at an estimate of \approx 10^4 ribosomes needed per cell to replicate
417 the entire protein mass (*Figure 8*). This point estimate and the corresponding estimate across a continuum of
418 growth rates proves to be notably comparable to the experimental observations, shown in *Figure 8(B)*. While the
419 ribosome is responsible for the formation of peptide bonds, we do not diminish the importance of the charging of
420 tRNAs with the appropriate amino acid, a process with occurs with remarkable accuracy. In the Appendix and in
421 *Figure 8–Figure Supplement 1*, we consider the process of ligating tRNAs to their corresponding amino acid and
422 again find notable comparability with the data.

423 Having completed our circuit through key processes of cellular growth outlined in *Figure 1*, we can now take
424 stock on our understanding of the observed growth rate dependence and abundances of various protein com-
425 plexes. We note that in general, these simple estimates have been reasonably successful in quantitatively describ-
426 ing the observations in the proteomic data, suggesting that the proteome is tuned in composition and absolute
427 abundance to match the growth rate requirements, without any one process representing a particular bottleneck
428 or rate limiting step in division. However, in our effort to identify key limitations on growth, there are two notable
429 observations that we wish to emphasize.

430 The first is a recurring theme throughout our estimates, which is that any inherent biochemical rate limitation
431 can be overcome by expressing more proteins. We can view this as a parallelization of each biosynthesis task,
432 and helps explain why bacteria tend to increase their protein content (and cell size) as growth rate increases
433 (Ojkic et al., 2019). The second, and ultimately the most significant in defining the cellular growth rate, is that the

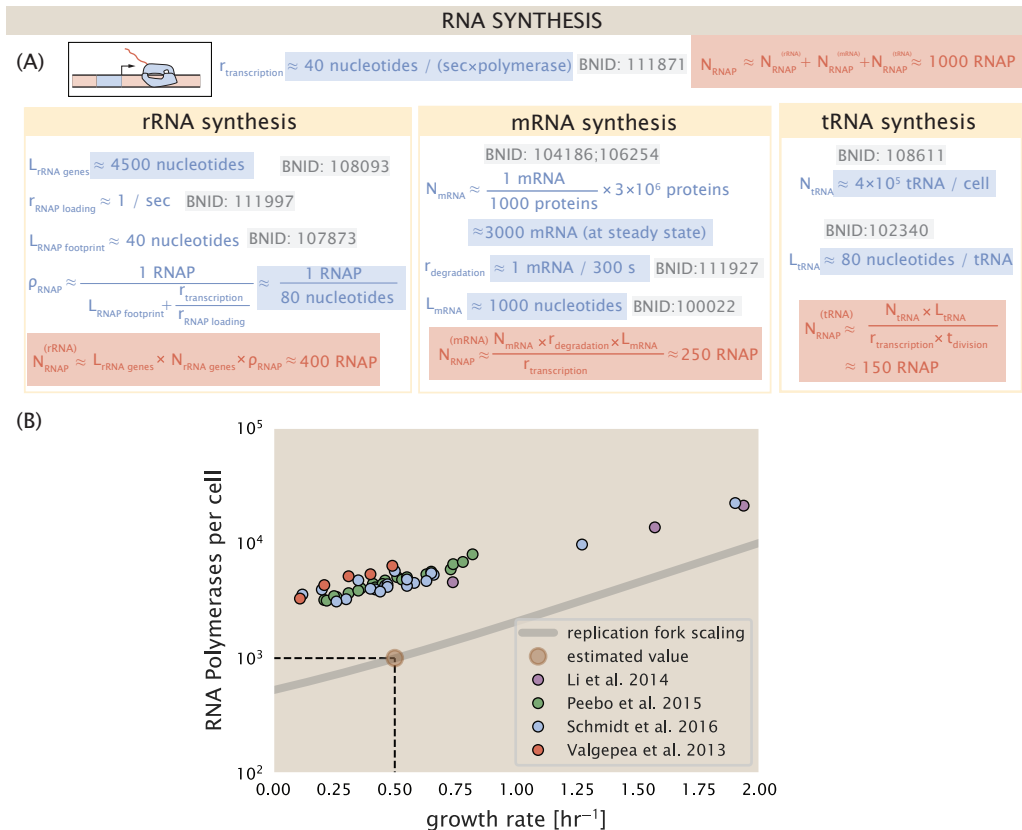


Figure 7. Estimation of the RNA polymerase demand and comparison with experimental data. (A) Estimations for the number of RNA polymerase needed to synthesize sufficient quantities of rRNA, mRNA, and tRNA from left to right, respectively. (B) The RNA polymerase core enzyme copy number as a function of growth rate. Colored points correspond to the average number RNA polymerase core enzymes that could be formed given a subunit stoichiometry of $[\text{RpoA}]_2[\text{RpoC}][\text{RpoB}]$.

Figure 7-Figure supplement 1. Abundance and growth rate dependence of σ -70.

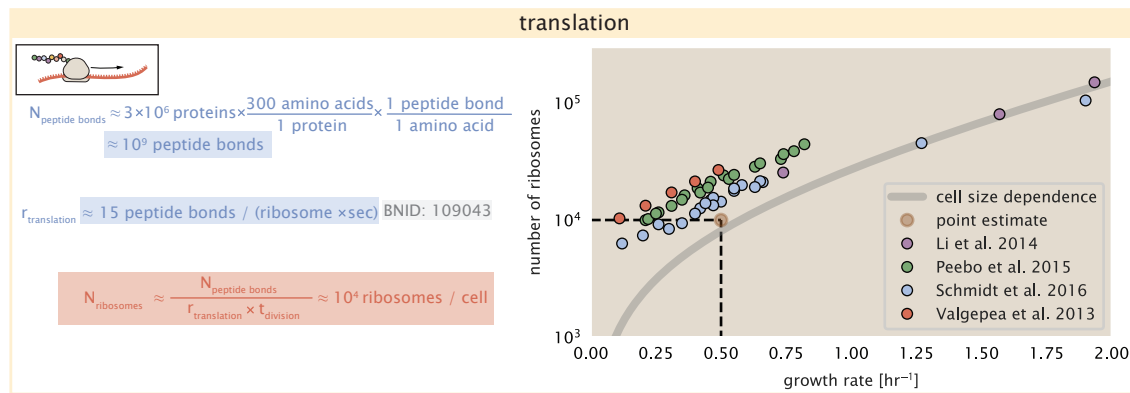


Figure 8. Estimation of the required number of ribosomes. Estimation of the number of ribosomes required to synthesize 10^9 peptide bonds with an elongation rate of 15 peptide bonds per second. The average abundance of ribosomes is plotted as a function of growth rate. Our estimated values are shown for a growth rate of 0.5 hr^{-1} . Grey lines correspond to the estimated complex abundance calculated at different growth rates.

Figure 8–Figure supplement 1. Estimate and observed abundance and growth rate dependence of tRNA ligases.

434 synthesis of ribosomal proteins presents a special case where parallelization is *not* possible and thereby imposes a
 435 limit on the fastest possible growth rate. This poses an optimization problem for the cell – how are the translational
 436 demands of the entire proteome met without investing resources in the production an excess of ribosomes? *just*
 437 the ribosomal fraction.

438 This question, more frequently presented as a question of optimal resource allocation, has been the target of
 439 an extensive dialogue between experiment and theory over the past decade. In a now seminal work, *Scott et al.*
 440 (2010) presents an elegant treatment of resource allocation through partitioning of the proteome into sectors –
 441 one of which being ribosome-associated proteins – the relative sizes of which ultimately define the total cellular
 442 growth rate. In more recent years, this view has been more thoroughly dissected experimentally (*Klumpp and Hwa, 2014; Basan et al., 2015; Dai et al., 2018, 2016; Erickson et al., 2017*) and together represent a paradigm-
 443 shift in how we think of cellular physiology at the proteome-level. However, the quantitative description of these
 444 observations is often couched in terms of phenomenological constants and effective parameters with the key
 445 observable features of expression being computed in relative, rather than absolute, abundances. Furthermore,
 446 these approaches often exclude or integrate away effects of cell size and chromosome content, which we have
 447 illustrated in our estimates to have deep connections to the observed cellular growth rate.
 448

449 In the closing sections of this work, we explore how ribosome content, cell size, and chromosome content are
 450 intertwined in their control over the cellular growth rate. To do so, we take a more detailed view of ribosome
 451 abundance, exchanging our order-of-magnitude estimates for a minimal mathematical model of growth rate con-
 452 trol defined by parameters with tangible connections to the biological processes underlying cellular growth. Using
 453 this model, we interrogate how the size of the ribosome pool and its corresponding activity is regulated to balance
 454 the supply of amino acids via metabolism and catabolism with consumption of amino acids through peptide bond
 455 formation.

456 Maximum Growth Rate is Determined by the Ribosomal Mass Fraction

457 To gain some intuition into how ribosomal synthesis influences bacterial growth, we again consider the total num-
 458 ber of peptide bonds that must be synthesized, which we denote as N_{pep} . With cells growing exponentially in time
 459 (*Godin et al., 2010*), the rate of cellular growth will be related to the rate of protein synthesis by

$$N_{\text{pep}} \lambda = r_i R f_a, \quad (1)$$

460 where λ is the cell growth rate, r_i is the maximum elongation rate in AA per second, and R is the average ribosome
 461 copy number per cell. The multiplicative factor f_a refers to the fraction of ribosomes actively translating, and
 462 allows us to account for the possibility of nonfunctional, immature ribosomes or active sequestration of ribosomes,

463 mediated by the secondary-messenger molecule alarmones, such as guanosine pentaphosphate [(p)ppGpp] at
464 slow growth (*Dennis et al., 2004; Dai et al., 2016*).

465 Rather than speaking in terms of absolute ribosome abundance, we can account for the ribosome content as
466 was defined by *Scott et al. (2010)* as the mass of fraction of the proteome occupied by ribosomes Φ_R . Similarly,
467 as N_{pep} is related to the total protein mass through the molecular weight of each protein, we can also consider
468 the growth rate in terms of the fraction of the total proteome mass dedicated to ribosomal proteins. By making
469 the approximation that an average amino acid has a molecular weight of 110 Da (BNID: 104877), the total protein
470 mass m_{protein} is related to N_{pep} by $(m_{\text{protein}}/110 \text{ Da}) \times N_A$, where N_A is Avogadro's number. Similarly, R is related
471 to the ribosomal protein mass by $R \approx (m_R/800 \text{ Da}) \times N_A$, where 800 Da reflects the summed molecular weight of
472 all ribosomal subunits. This allows us to approximate $R/N_{\text{pep}} \approx \Phi_R/L_R$, where Φ_R is the ribosomal mass fraction
473 m_{protein}/m_R , and L_R the ratio of 800 kDa / 110 Da per amino acid or, alternatively, the total length in amino acids
474 that make up a ribosome. Under this parameterization, the translation-limited growth rate can then be written in
475 the form

$$\lambda_{\text{translation-limited}} \approx \frac{r_t}{L_R} \Phi_R f_a. \quad (2)$$

476 This is plotted as a function of the ribosomal fraction Φ_R in the top panel of *Figure 9(A)*, where we take $L_R \approx$
477 7500 AA, corresponding to the length in amino acids for all ribosomal subunits of the 50S and 30S complex (BNID:
478 101175), and $f_a = 1$. To compare this relationship to the proteomic data, we make use of recent measurements of
479 f_a from *Dai et al. (2016)* (*Figure 9(A)*, bottom inset) to estimate the active fraction of ribosomal protein across each
480 proteomic data set (*Figure 9(A)*, colored points, bottom). In general, the data appear to skirt this limit in growth
481 rate as nutrient conditions vary. There is a notable discrepancy in the data from *Peebo et al. (2015); Valgepea*
482 *et al. (2013)*, where cells appear to grow substantially slower given their estimated ribosomal fraction. Here we
483 have also collected a number of recent non-proteomic measurements of ribosomal fraction and find them most
484 consistent with the measurements from *Li et al. (2014); Schmidt et al. (2016)* (gray points; also see *Figure 9–Figure*
485 *Supplement 1(A)*).

486 The growth rate defined by *Equation 2* reflects mass-balance under steady state growth and has long provided
487 a rationalization of the apparent linear increase in *E. coli*'s ribosomal content as a function of growth rate (*Maaløe,*
488 *1979; Scott et al., 2010*). The maximum rate, when $\Phi_R = 1$, could only be achieved if a cell contained only ribo-
489 somes (*Dill et al., 2011*). This corresponds to the synthesis time of all ribosomal subunits, $L_R/r_t \approx 7$ minutes and
490 interestingly, is independent of the absolute number of ribosomes (*Figure 9(B)*). To return to our earlier comments
491 on parallelization, it is this step that is rate-limiting, with each ribosome being required to produce a second ribo-
492 some. Unless elongation rate increased, or cells could trim their total ribosomal protein mass, this dependency
493 limits both the maximum growth rate (when $\Phi_R = 1$), and also the achievable growth rate under more moderate
494 values of Φ_R .

495 rRNA Synthesis Presents a Potential Bottleneck during Rapid Growth

496 *E. coli* rarely exhibits growth rates above 2 hr^{-1} (*Bremer and Dennis, 2008*), which is still well-below the synthesis
497 rate of a single ribosome, and below the growth rates reported for several other bacteria (*Roller et al., 2016*). Here
498 we need to also consider ribosomal synthesis from the perspective of limiting rRNA synthesis, which as we have
499 found earlier, will depend on the number of rRNA operons to transcribe rRNA.

500 Due to multiple rounds of chromosomal replication per cell doubling, the effective number of rRNA operons
501 increases with growth rate and will vary in proportion to the average number of origins per cell, $\langle \# \text{ ori} \rangle$. This
502 parameter is set by how often replication must be initiated per cell doubling in order to maintain steady state
503 growth, and quantified by

$$\langle \# \text{ ori} \rangle = 2^{\tau_{\text{cyc}}/\tau} = 2^{\tau_{\text{cyc}} \lambda / \ln(2)}. \quad (3)$$

504 Here, τ_{cyc} is the cell cycle time (referring to the time from replication initiation to cell division), and τ is the cell
505 doubling time. We used the experimental measurements of τ_{cyc} and τ from *Si et al. (2017)* (*Figure 9–Figure*
506 *Supplement 1(B)*) to calculate $\langle \# \text{ ori} \rangle$ with *Equation 3* as a function of growth rates. For growth rates above about
507 0.5 hr^{-1} , τ_{cyc} is approximately constant at about 70 minutes, which means that $\langle \# \text{ ori} \rangle$ will grow exponentially
508 with growth rate. Since the rRNA operons are predominantly located near to origin of replication (BNID: 100352,

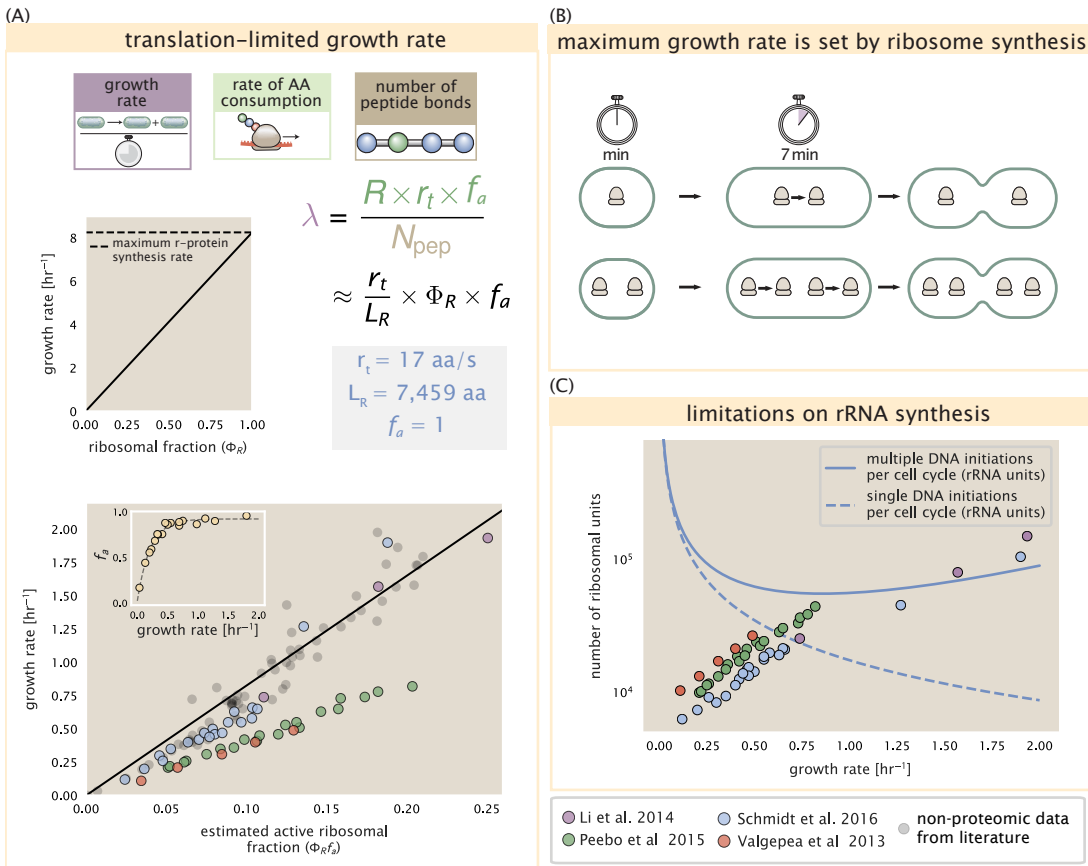


Figure 9. Translation-limited growth rate. (A) top: Translation-limited growth as a function of the ribosomal fraction. The solid line is calculated for an elongation rate of 17 aa per second. The dashed line corresponds to the maximum rate of ribosomal protein (R-protein) synthesis considered in part (C). bottom: Actively translating ribosomal fraction versus growth rate. The actively translating ribosomal fraction is calculated using the estimated values of f_a from [Dai et al. \(2016\)](#) (shown in inset; see Appendix Calculation of active ribosomal fraction for additional detail). Gray data points show additional measurements from literature and consider further in [Figure 9–Figure Supplement 1\(A\)](#). (B) An inherent maximum growth rate is set by the time to synthesize all ribosomal subunits. This growth rate is given by r_t / L_R , where r_t is the elongation rate and L_R is the total number of amino acids that make up the entire ribosomal complex. This rate is independent of the number of ribosomes and instead is limited by the time required to double an individual ribosome. (C) Maximum number of rRNA units that can be synthesized as a function of growth rate. Solid curve corresponding to the rRNA copy number is calculated by multiplying the number of rRNA operons by the estimated number of (# ori) at each growth rate. The quantity (# ori) was calculated using Equation 4 and the measurements from [Si et al. \(2017\)](#) that are plotted in [Figure 10\(A\)](#). The dashed line shows the maximal number of functional rRNA units produced from a single chromosomal initiation per cell cycle.

Figure 9–Figure supplement 1. Comparison of $\Phi_R f_a$ with literature and estimation of (# ori).

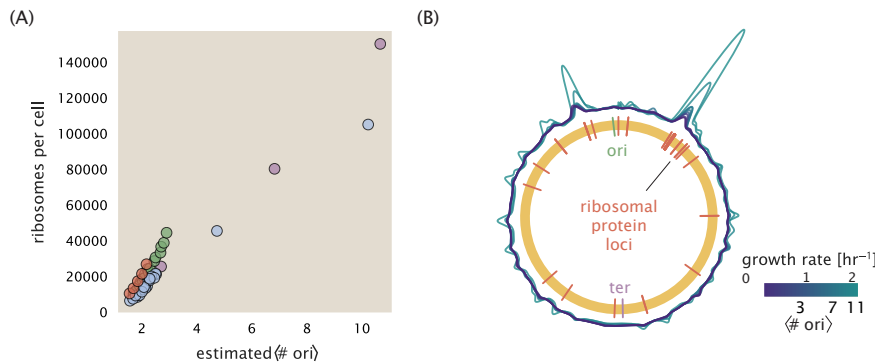


Figure 10. Cells increase both absolute ribosome abundance and Φ_R with $\langle \# \text{ori} \rangle$. (A) Plot of the ribosome copy number estimated from the proteomic data against the estimated $\langle \# \text{ori} \rangle$ (see Appendix Estimation of $\langle \# \text{ori} \rangle / \langle \# \text{ter} \rangle$ and $\langle \# \text{ori} \rangle$ for additional details). (B) A running Gaussian average (20 kbp st. dev.) of protein copy number is calculated for each growth condition considered by (Schmidt et al., 2016) based on each gene's transcriptional start site. Since total protein abundance increases with growth rate, protein copy numbers are median-subtracted to allow comparison between growth conditions. $\langle \# \text{ori} \rangle$ are estimated using the data in (A) and Equation 3.

509 Dennis et al. (2004)), we make the simplifying assumption that the number of rRNA operons will be directly
510 proportional to $\langle \# \text{ori} \rangle$.

511 Returning to our rule-of-thumb of 1 functional rRNA unit per second per operon, we estimate the maximum
512 number of ribosomes that could be made as a function of growth rate (Figure 9(C), blue curve). Although we
513 expect this estimate to drastically overestimate rRNA abundance at slower growth rates ($\lambda < 0.5 \text{ hr}^{-1}$), it provides
514 a useful reference alongside the proteomic measurements. For growth rates above about 1 hr^{-1} , we find that cells
515 will need to transcribe rRNA near their maximal rate. As a counter example, if *E. coli* did not initiate multiple rounds
516 of replication, they would be unable to make enough rRNA for the observed number of ribosomes (dashed blue
517 curve in Figure 9(C)). The convergence between the maximum rRNA production and measured ribosome copy
518 number suggests rRNA synthesis may begin to present a bottleneck at the fastest growth rates due to the still-
519 limited copies of rRNA genes.

520 Rapid Growth Requires *E. coli* to Increase Both Cell Size and Ribosomal Mass Fraction

521 In Figure 9(C) we find that above about 0.75 hr^{-1} , the growth rate is determined by the ribosomal mass fraction
522 Φ_R , since f_a is close to 1, and r_t is near its maximal rate [cite and refer to figure/ supplemental]. While Φ_R will need
523 to increase in order for cells to grow faster, the fractional dependence in Equation 2 gives little insight into how
524 this is actually achieved in the cell and we consider this further here.

525 It is now well-documented that *E. coli* cells add a constant volume per origin of replication, which is robust to
526 a remarkable array of cellular perturbations (Si et al., 2017). We find that ribosomal copy number also scales its
527 ribosome copy number in proportion to $\langle \# \text{ori} \rangle$ Figure 10(A). Importantly, however, it will only be due to an increase
528 in Φ_R at these moderate to fast growth rates that cells can achieve an increase in their growth rate. Indeed, we
529 find that the deviations in protein expression with $\langle \# \text{ori} \rangle$ are largely restricted to regions of ribosomal protein
530 genes Figure 10(B). Here we have calculated the position-dependent protein expression across the chromosome
531 by a running Gaussian average of protein copy number (20 kbp st. dev. averaging window) based on each gene's
532 transcriptional start site. These were median-subtracted to account for the change in total protein abundance
533 with $\langle \# \text{ori} \rangle$. This result suggests that Φ_R is also being tuned in proportion to $\langle \# \text{ori} \rangle$ under nutrient-limited growth,
534 and in particular, it is through this additional dependence on Φ_R that *E. coli* exhibits an exponential increase in cell
535 size with growth rate.

536 A Minimal Model of Nutrient-Mediated Growth Rate Control

537 While the preceding subsections highlight a dominant role for ribosomes in setting the growth rate, our analysis
538 on the whole emphasizes that the total proteomic content must also change in response to variable growth con-

ditions and growth rate. In this final section we use a minimal model of growth rate control to better understand how the interconnection between ribosomal abundance and total protein influences the observed growth rate.

Here we propose that cells modulate their protein abundance in direct response to the availability of nutrients in their environment. As noted earlier, bacteria can modulate ribosomal activity through the secondary-messenger molecules like (p)ppGpp in poorer nutrient conditions (*Figure 9(C)* - inset; *Dai et al. (2016)*). Importantly, these secondary-messengers also cause global changes in transcriptional and translational activity (*Hauryliuk et al., 2015; Zhu and Dai, 2019; Büke et al., 2020*). In *E. coli*, amino acid starvation leads to the accumulation of deacylated tRNAs at the ribosome's A-site and a strong increase in (p)ppGpp synthesis activity by the enzyme RelA (*Hauryliuk et al., 2015*). Along with this, there is increasing evidence that (p)ppGpp also acts to inhibit the initiation of DNA replication (*Kraemer et al., 2019*), providing a potential mechanism to lower $\langle \# \text{ ori} \rangle$ and maintain a smaller cell size in poorer growth conditions (*Fernández-Coll et al., 2020*).

To consider this quantitatively, we assume that cells modulate their proteome (N_{pep} , R , Φ_R) to better maximize their rate of peptide elongation r_t . The elongation rate r_t will depend on how quickly the ribosomes can match codons with their correct amino-acyl tRNA, along with the subsequent steps of peptide bond formation and translocation. This ultimately depends on the cellular concentration amino acids, which we treat as a single effective species, $[AA]_{\text{eff}}$. In our model, we determine the the rate of peptide elongation r_t and achievable growth rate as simply depending on the supply of amino acids (and, therefore, also amino-acyl tRNAs), through a parameter r_{AA} in units of AA per second, and the rate of amino acid consumption by protein synthesis ($r_t \times R \times f_a$). This is shown schematically in *Figure 11(A)* and derived in Appendix ???. Given our observation that protein synthesis and energy production are not limiting, we assume that other molecular players required by ribosomes like elongation factors and GTP are available in sufficient abundance.

In *Figure 11(B)*, we illustrate how the elongation rate will depend on the ribosomal copy number. Here, we have considered an arbitrarily chosen $r_{AA} = 5 \times 10^6 \text{ AA} \cdot \text{s}^{-1} \cdot \mu\text{m}^{-3}$ and $f_a = 1$ for a unit cell volume $V = 1\text{fL}$. At low ribosome copy numbers, the observed elongation rate is dependent primarily on $[AA]_{\text{eff}}$ through r_{AA} [as $r_t^{\max} \times R \times f_a \ll r_{AA}$, point (1) in *Figure 11(B)*]. As the ribosome copy number is increased such that the amino acid supply rate and consumption rate are nearly equal [point (2) in *Figure 11(B)*], the observed elongation rate begins to decrease sharply. When the ribosome copy number is increased even further, consumption at the maximum elongation rate exceeds the supply rate, yielding a significantly reduced elongation rate [point (3) in *Figure 11B*]. While the elongation rate will always be dominated by the amino acid supply rate at sufficiently low ribosome copy numbers, the elongation rate at larger ribosome abundances can be increased by tuning f_a such that not all ribosomes are elongating, reducing the total consumption rate.

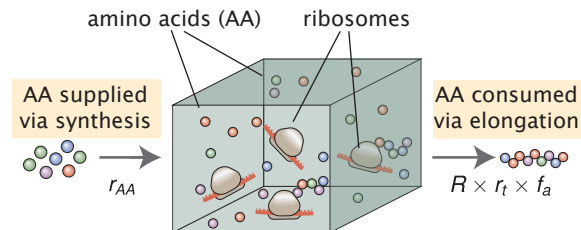
Optimal Ribosomal Content and Cell Size Depend on Nutrient Availability and Metabolic Capacity

To relate elongation rate to growth rate, we constrain the set of parameters based on our available proteomic measurements; namely, we restrict the values of R , N_{pep} , and cell size to those associated with the amalgamated proteomic data (described in Appendix Estimation of Total Protein Content per Cell). We then consider how changes in the nutrient conditions, through the parameter r_{AA} , influence the maximum growth rate as determined by ???. *Figure 11(C)* shows how the observed growth rate depends on the rate of amino acid supply r_{AA} as a function of the cellular ribosome copy number. A feature immediately apparent is the presence of a maximal growth rate whose dependence on R (and consequently, the cell size) increases with increasing r_{AA} . Importantly, however, there is an optimum set of R , N_{pep} , and V that are strictly dependent on the value of r_{AA} . Increasing the ribosomal concentration beyond the cell's metabolic capacity has the adverse consequence of depleting the supply of amino acids and a concomitant decrease in the elongation rate r_t , [*Figure 11(B)*].

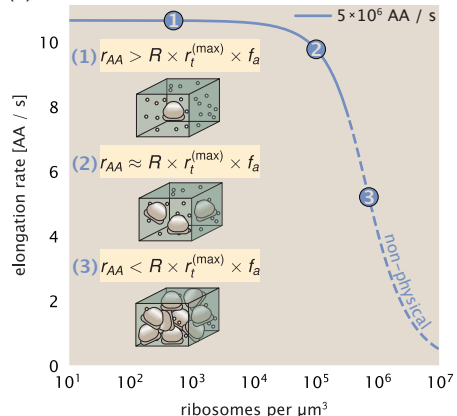
Also of note is the growth rate profiles shown for low amino acid supply rates [purple and blue lines in *Figure 11(C)*], representing growth in nutrient-poor media. In these conditions, there no longer exists a peak in growth, at least in the range of physiologically-relevant ribosome copy numbers. Instead, cells limit their pool of actively translating ribosomes by decreasing f_a (*Dai et al., 2016*), which would help maintain the pool of available amino acids $[AA]_{\text{eff}}$ and increase the achievable elongation rate. This observation is in agreement with the central premise of the cellular resource allocation principle proposed by *Scott et al. (2010); Klumpp et al. (2009); Klumpp and Hwa (2014)* and *Hui et al. (2015)*.

(A)

A MINIMAL MODEL FOR NUTRIENT-LIMITED GROWTH



(B)



(C)

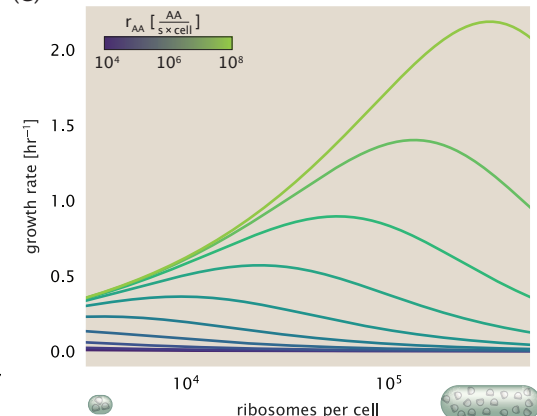


Figure 11. A minimal model of growth rate control under nutrient limitation. (A) We consider a unit volume of cellular material composed of amino acids (colored spheres) provided at a supply rate r_{AA} . These amino acids are polymerized by a pool of ribosomes (brown blobs) at a rate $r_t \times R \times f_a$, where r_t is the elongation rate, R is the ribosome copy number in the unit volume, and f_a is the fraction of those ribosomes actively translating. (B) The observed elongation rate is plotted as a function of ribosomes. The three points correspond to three regimes of ribosome copy numbers and are shown schematically on the left-hand side. The region of the curve shown as dashed lines represents a non-physical copy number, but is shown for illustrative purposes. This curve was generated using the parameters $r_{AA} = 5 \times 10^6 \text{ AA / s}$, $r_t^{(\max)} = 17.1 \text{ AA / s}$, $f_a = 1$, and a unit cell volume of $V = 1\text{fL}$. See Appendix ?? for additional model details. (C) The cellular growth rate is plotted as a function of total cellular ribosome copy number for different cellular amino acid supply rates, with blue and green curves corresponding to low and high supply rates, respectively. As the ribosome copy number is increased, so too is the cell size and total protein abundance N_{pep} . We direct the reader to the Suppmental Information for discussion on the inference of the realtionship between cell size, number of peptide bonds, and ribosome copy number.

588 **Discussion**

589 Continued experimental and technological improvements have led to a treasure trove of quantitative biological
590 data ([Hui et al., 2015](#); [Schmidt et al., 2016](#); [Si et al., 2017](#); [Gallagher et al., 2020](#); [Peebo et al., 2015](#); [Valgepea et al.,
591 2013](#)), and an ever advancing molecular view and mechanistic understanding of the constituents that support
592 bacterial growth ([Taheri-Araghi et al., 2015](#); [Morgenstein et al., 2015](#); [Si et al., 2019](#); [Karr et al., 2012](#); [Kostinski and
593 Reveni, 2020](#)). In this work we have compiled what we believe to be the state-of-the-art knowledge on proteomic
594 copy number across a broad range of growth conditions in *E. coli*. We have made this data accessible through a
595 [GitHub repository](#), and an interactive figure that allows exploration of specific protein and protein complex copy
596 numbers. Through a series of order-of-magnitude estimates that traverse key steps in the bacterial cell cycle, this
597 proteomic data has been a resource to guide our understanding of two key questions: what biological processes
598 limit the absolute speed limit of bacterial growth, and how do cells alter their molecular constituents as a function
599 of changes in growth rate or nutrient availability? While not exhaustive, our series of estimates provide insight
600 on the scales of macromolecular complex abundance across four classes of cellular processes – the transport of
601 nutrients, the production of energy, the synthesis of the membrane and cell wall, and the numerous steps of the
602 central dogma.

603 In general, the copy numbers of the complexes involved in these processes were reasonable agreement with
604 our order-of-magnitude estimates. Since many of these estimates represent soft lower-bound quantities, this
605 suggests that cells do not express proteins grossly in excess of what is needed for a particular growth rate. Several
606 exceptions, however, also highlight the dichotomy between a proteome that appears to "optimize" expression
607 according to growth rate and one that must be able to quickly adapt to environments of different nutritional quality.
608 Take, for example, the expression of carbon transporters. Shown in [Figure 2\(B\)](#), we find that cells always express
609 a similar number of glucose transporters irrespective of growth condition. At the same time, it is interesting to
610 note that many of the alternative carbon transporters are still expressed in low but non-zero numbers (≈ 10 -
611 100 copies per cell) across growth conditions. This may relate to the regulatory configuration for many of these
612 operons, which require the presence of a metabolite signal in order for alternative carbon utilization operons to
613 be induced ([Monod, 1949](#); [Laxhuber et al., 2020](#)). Furthermore, upon induction, these transporters are expressed
614 and present in abundances in close agreement with a simple estimate.

615 Of the processes illustrated in [Figure 1](#), we arrive at a ribosome-centric view of cellular growth rate control.
616 This is in some sense unsurprising given the long-held observation that *E. coli* and many other organisms vary
617 their ribosomal abundance as a function of growth conditions and growth rate ([Scott et al., 2010](#); [Metzl-Raz et al.,
618 2017](#)). However, through our dialogue with the proteomic data, two additional key points emerge. The first relates
619 to our question of what process sets the absolute speed limit of bacterial growth. While a cell can parallelize
620 many of its processes simply by increasing the abundance of specific proteins or firing multiple rounds of DNA
621 replication, this is not so for synthesis of ribosomes ([Figure 9\(A\)](#)). The translation time for each ribosome [≈ 7 min,
622 [Dill et al. \(2011\)](#)] places an inherent limit on the growth rate that can only be surpassed if the cell were to increase
623 their polypeptide elongation rate, or if they could reduce the total protein and rRNA mass of the ribosome. The
624 second point relates to the long-observed correlations between growth rate and cell size ([Schaechter et al., 1958](#); [Si
625 et al., 2017](#)), and between growth rate and ribosomal mass fraction. While both trends have sparked tremendous
626 curiosity and driven substantial amounts of research in their own regards, these relationships are themselves
627 intertwined. In particular, it is the need for cells to increase their absolute number of ribosomes under conditions
628 of rapid growth that require cells to also grow in size. Further experiments are needed to test the validity of this
629 hypothesis. In particular, we believe that the change in growth rate in response to translation-inhibitory drugs
630 (such as chloramphenicol) could be quantitatively predicted, given one had precision measurement of the relevant
631 parameters, including the fraction of actively translating ribosomes f_a and changes in the metabolic capacity of
632 the cell (i.e. the parameter r_{AA} in our minimal model) for a particular growth condition.

633 While the generation of new ribosomes plays a dominant role in growth rate control, there exist other physical
634 limits to the function of cellular processes. One of the key motivations for considering energy production was
635 the physical constraints on total volume and surface area as cells vary their size ([Harris and Theriot, 2018](#); [Ojkic
636 et al., 2019](#)). While *E. coli* get larger as it expresses more ribosomes, an additional constraint begins to arise in
637 energy production due to a relative decrease in total surface area where ATP is predominantly produced ([Szenk](#)

638 *et al., 2017*). Specifically, the cell interior requires an amount of energy that scales cubically with cell size, but
639 the available surface area only grows quadratically (*Figure 5(A)*). While this threshold does not appear to be met
640 for *E. coli* cells growing at 2 hr⁻¹ or less, it highlights an additional constraint on growth given the apparent need
641 to increase in cell size to grow faster. This limit is relevant even to eukaryotic organisms, whose mitochondria
642 exhibit convoluted membrane structures that nevertheless remain bacteria-sized organelles (*Guo et al., 2018*). In
643 the context of bacteria growth and energy production more generally, we have limited our analysis to the aerobic
644 growth conditions associated with the proteomic data and further consideration will be needed for anaerobic
645 growth.

646 This work is by no means meant to be an exhaustive dissection of bacterial growth rate control, and there are
647 many aspects of the bacterial proteome and growth that we neglected to consider. For example, other recent work
648 (*Liebermeister et al., 2014; Hui et al., 2015; Schmidt et al., 2016*) has explored how the proteome is structured
649 and how that structure depends on growth rate. In the work of *Hui et al. (2015)*, the authors coarse-grained the
650 proteome into six discrete categories being related to either translation, catabolism, anabolism, and others related
651 to signaling and core metabolism. The relative mass fraction of the proteome occupied by each sector could be
652 modulated by external application of drugs or simply by changing the nutritional content of the medium. While we
653 have explored how the quantities of individual complexes are related to cell growth, we acknowledge that higher-
654 order interactions between groups of complexes or metabolic networks at a systems-level may reveal additional
655 insights into how these growth-rate dependences are mechanistically achieved. Furthermore, while we anticipate
656 the conclusions summarized here are applicable to a wide collection of bacteria with similar lifestyles as *E. coli*,
657 other bacteria and archaea may have evolved other strategies that were not considered. Further experiments
658 with the level of rigor now possible in *E. coli* will need to be performed in a variety of microbial organisms to learn
659 more about how regulation of proteomic composition and growth rate control has evolved over the past 3.5 billion
660 years.

661 Methods

662 Data Analysis and Availability

663 All proteomic measurements come from the experimental work of *Schmidt et al. (2016); Peebo et al. (2015); Val-*
664 *gepea et al. (2013)* (mass spectrometry) and *Li et al. (2014)* (ribosomal profiling). Data curation and analysis was
665 done programmatically in Python, and compiled data and analysis files are accessible through a [GitHub reposi-
666 tory] (DOI:XXX) associated with this paper as well as on the associated [paper website](#). An interactive figure that
667 allows exploration of specific protein and protein complex copy numbers is available at [link].

668 Acknowledgements

669 We thank Matthias Heinemann, Alexander Schmidt, and Gene-Wei Li for additional input regarding their data. We
670 also thank members of the Phillips, Theriot, Kondev, and Garcia labs for useful discussions. R.P. is supported by
671 La Fondation Pierre-Gilles de Gennes, the Rosen Center at Caltech, and the NIH 1R35 GM118043 (MIRA). J.A.T. is
672 supported by the Howard Hughes Medical Institute, and NIH Grant R37-AI036929. N.M.B is a HHMI Fellow of The
673 Jane Coffin Childs Memorial Fund.

674 Competing Interests

675 The authors declare no competing interests.

⁶⁷⁶ **Appendix for: Fundamental limits on the**
⁶⁷⁷ **rate of bacterial cell division**

⁶⁷⁸ **Nathan M. Belliveau^{†, 1}, Griffin Chure^{†, 2}, Christina L. Hueschen³, Hernan G. Garcia⁴, Jane**
⁶⁷⁹ **Kondev⁵, Daniel S. Fisher⁶, Julie A. Theriot^{1, 7, *}, Rob Phillips^{8, 9, *}**

⁶⁸⁰ ¹Department of Biology, University of Washington, Seattle, WA, USA; ²Department of Applied Physics,
⁶⁸¹ California Institute of Technology, Pasadena, CA, USA; ³Department of Chemical Engineering,
⁶⁸² Stanford University, Stanford, CA, USA; ⁴Department of Molecular Cell Biology and Department of
⁶⁸³ Physics, University of California Berkeley, Berkeley, CA, USA; ⁵Department of Physics, Brandeis
⁶⁸⁴ University, Waltham, MA, USA; ⁶Department of Applied Physics, Stanford University, Stanford, CA,
⁶⁸⁵ USA; ⁷Allen Institute for Cell Science, Seattle, WA, USA; ⁸Division of Biology and Biological Engineering,
⁶⁸⁶ California Institute of Technology, Pasadena, CA, USA; ⁹Department of Physics, California Institute of
⁶⁸⁷ Technology, Pasadena, CA, USA; *Co-corresponding authors. Address correspondence to
⁶⁸⁸ phillips@pboc.caltech.edu and jtheriot@uw.edu; [†]These authors contributed equally to this work

689	Contents	
690	Introduction	1
691	Nutrient Transport	2
692	Limits on Transporter Expression	6
693	Cell Envelope Biogenesis	6
694	Lipid Synthesis	6
695	Peptidoglycan Synthesis	7
696	Limits on Cell Wall Biogenesis	7
697	Energy Production	7
698	ATP Synthesis	9
699	Generating the Proton Electrochemical Gradient	9
700	Limits on Biosynthesis in a Crowded Membrane	11
701	Processes of the Central Dogma	11
702	DNA Replication	11
703	RNA Synthesis	13
704	Protein Synthesis	14
705	Maximum Growth Rate is Determined by the Ribosomal Mass Fraction	16
706	rRNA Synthesis Presents a Potential Bottleneck during Rapid Growth	17
707	Rapid Growth Requires <i>E. coli</i> to Increase Both Cell Size and Ribosomal Mass Fraction	19
708	A Minimal Model of Nutrient-Mediated Growth Rate Control	19
709	Optimal Ribosomal Content and Cell Size Depend on Nutrient Availability and Metabolic Capacity	20
710	Discussion	22
711	Methods	23
712	Data Analysis and Availability	23
713	Acknowledgements	23
714	Competing Interests	23
715	Experimental Details Behind Proteomic Data	27
716	Fluorescence based measurements	27
717	Ribosomal profiling measurements	27
718	Mass spectrometry measurements	28
719	Summary of Proteomic Data	28
720	Estimation of Cell Size and Surface Area	29
721	Estimation of Total Protein Content per Cell	31
722	Estimating Volume and Number of Amino Acids from Ribosome Copy Number	31
723	Additional Considerations of Schmidt <i>et al.</i> Data Set	31
724	Effect of cell volume on reported absolute protein abundances	33
725	Relaxing assumption of constant protein concentration across growth conditions	35
726	Comparison with total protein measurements from Basan <i>et al.</i> 2015.	35
727	Calculation of Complex Abundance	36

728	Extending Estimates to a Continuum of Growth Rates	38
729	Estimation of the total cell mass	38
730	Complex Abundance Scaling With Cell Volume	38
731	A Relation for Complex Abundance Scaling With Surface Area	39
732	Number of Lipids	39
733	Number of Murein Monomers	39
734	Complex Abundance Scaling With Number of Origins, and rRNA Synthesis	40
735	Calculation of active ribosomal fraction.	40
736	Estimation of $\langle \#ori \rangle / \langle \#ter \rangle$ and $\langle \#ori \rangle$.	40

Table 1. Overview of proteomic data sets.

Author	Method	Reported Quantity
Taniguchi <i>et al.</i> (2010)	YFP-fusion, cell fluorescence	fg/copies per cell
Valgepea <i>et al.</i> (2012)	mass spectrometry	fg/copies per cell
Peebo <i>et al.</i> (2014)	mass spectrometry	fg/copies per fl
Li <i>et al.</i> (2014)	ribosomal profiling	fg/copies per cell ^a
Soufi <i>et al.</i> (2015)	mass spectrometry	fg/copies per cell
Schmidt <i>et al.</i> (2016)	mass spectrometry	fg/copies per cell ^b

a. The reported values assume that the proteins are long-lived compared to the generation time but are unable to account for post-translational modifications that may alter absolute protein abundances.

b. This mass spectrometry approach differs substantially from the others since in addition to the relative proteome-wide abundance measurements, the authors performed absolute quantification of 41 proteins across all growth conditions (see Section Additional Considerations of Schmidt *et al.* Data Set for more details on this).

737 Experimental Details Behind Proteomic Data

738 Here we provide a brief summary of the experiments behind each proteomic data set. The purpose of this section
739 is to identify how the authors arrived at absolute protein abundances. In the following section (Section Summary
740 of Proteomic Data) we will then provide a summary of the final protein abundance measurements that were
741 used throughout the main text. Table 1 provides an overview of the publications we considered. These are pre-
742 dominately mass spectrometry-based, with the exception of the work from Li *et al.* (2014) which used ribosomal
743 profiling, and the fluorescence-based counting done in Taniguchi *et al.* (2010).

744 Fluorescence based measurements

745 In the work of Taniguchi *et al.* (2010), the authors used a chromosomal YFP fusion library where individual strains
746 have a specific gene tagged with a YFP-coding sequence. 1018 of their 1400 attempted strains were used in the
747 work. A fluorescence microscope was used to collect cellular YFP intensities across all these strains. Through au-
748 tomated image analysis, the authors normalized intensity measurements by cell size to account for the change
749 in size and expression variability across the cell cycle. Following correction of YFP intensities for cellular autoflu-
750 orescence, final absolute protein levels were determined by a calibration curve with single-molecule fluorescence
751 intensities. This calibration experiment was performed separately using a purified YFP solution.

752 Ribosomal profiling measurements

753 The work of Li *et al.* (2014) takes a sequencing based approach to estimate protein abundance. Ribosomal pro-
754 filing, which refers to the deep sequencing of ribosome-protected mRNA fragments, can provide a quantitative
755 measurement of the protein synthesis rate. As long as the protein life-time is long relative to the cell doubling
756 time, it is possible to estimate absolute protein copy numbers. The absolute protein synthesis rate has units of
757 proteins per generation, and for stable proteins will also correspond to the protein copy number per cell.

758 In the experiments, ribosome-protected mRNA is extracted from cell lysate and selected on a denaturing poly-
759 acrylamide gel for deep sequencing (15–45 nt long fragments collected and sequenced by using an Illumina HiSeq
760 2000 in Li *et al.* (2014)). Counts of ribosome footprints from the sequencing data were then corrected empiri-
761 cally for position-dependent biases in ribosomal density across each gene, as well as dependencies on specific
762 sequences including the Shine-Dalgarno sequence. These data-corrected ribosome densities represent relative
763 protein synthesis rates. Absolute protein synthesis rates are obtained by multiplying the relative rates by the total
764 cellular protein per cell. The total protein per unit volume was determined with the Lowry method to quantify
765 total protein, calibrated against bovine serum albumin (BSA). By counting colony-forming units following serial
766 dilution of their cell cultures, they then calculated the total protein per cell.

767 **Mass spectrometry measurements**

768 Perhaps not surprisingly, the data is predominantly mass spectrometry based. This is largely due to tremendous
769 improvements in the sensitivity of mass spectrometers, as well as improvements in sample preparation and data
770 analysis pipelines. It is now a relatively routine task to extract protein from a cell and quantify the majority of
771 proteins present by shotgun proteomics. In general, this involves lysing cells, enzymatically digesting the proteins
772 into short peptide fragments, and then introducing them into the mass spectrometer (e.g. with liquid chromatog-
773 raphy and electrospray ionization), which itself can have multiple rounds of detection and further fragmentation
774 of the peptides.

775 Most quantitative experiments rely on labeling protein with stable isotopes, which allow multiple samples to
776 be measured together by the mass spectrometer. By measuring samples of known total protein abundance simul-
777 taneously (i.e. one sample of interest, and one reference), it is possible to determine relative protein abundances.
778 Absolute protein abundances can be estimated following the same approach used above for ribosomal profil-
779 ing, which is to multiply each relative abundance measurement by the total cellular protein per cell. This is the
780 approach taken by *Valgepea et al. (2013)* and *Peebo et al. (2015)*, with relative protein abundances determined
781 based on the relative peptide intensities (label free quantification 'LFQ' intensities). For the data of *Valgepea et al.*
782 (*2013*), total protein per cell was determined by measuring total protein by the Lowry method, and counting colony-
783 forming units following serial dilution. For the data from *Peebo et al. (2015)*, the authors did not determine cell
784 quantities and instead report the cellular protein abundances in protein per unit volume by assuming a mass
785 density of 1.1 g/ml, with a 30% dry mass fraction.

786 An alternative way to arrive at absolute protein abundances is to dope in synthetic peptide fragments of known
787 abundance. These can serve as a direct way to calibrate mass spectrometry signal intensities to absolute mass.
788 This is the approach taken by *Schmidt et al. (2016)*. In addition to a set of shotgun proteomic measurements to
789 determine proteome-wide relative abundances, the authors also performed absolute quantification of 41 proteins
790 covering over four orders of magnitude in cellular abundance. Here, a synthetic peptide was generated for each of
791 the proteins, doped into each protein sample, and used these to determine absolute protein abundances of the 41
792 proteins. These absolute measurements, determined for every growth condition, were then used as a calibration
793 curve to convert proteomic-wide relative abundances into absolute protein abundance per cell. A more extensive
794 discussion of the *Schmidt et al. (2016)* data set can be found in Section Additional Considerations of Schmidt et al.
795 Data Set.

796 **Summary of Proteomic Data**

797 In the work of the main text we only used the data from *Valgepea et al. (2013)*; *Li et al. (2014)*; *Peebo et al. (2015)*;
798 *Schmidt et al. (2016)*. As shown in *Figure 12(A)*, the reported total protein abundances in the work of *Taniguchi*
799 *et al. (2010)* and *Soufi et al. (2015)* differed quite substantially from the other work. For the work of *Taniguchi*
800 *et al. (2010)* this is in part due to a lower coverage in total proteomic mass quantified, though we also noticed that
801 most proteins appear undercounted when compared to the other data.

802 *Figure 12(B)* summarizes the total protein mass for each data point in our final compiled data set. We note that
803 protein abundances were all scaled so they followed a common growth rate-dependent change in total protein
804 mass. While our inclination initially was to leave reported copy numbers untouched, a notable discrepancy in the
805 scaling total protein per cell between *Schmidt et al. (2016)* and the other data sets forced us to dig deeper into
806 those measurements (compare *Schmidt et al. (2016)* and *Li et al. (2014)* data in *Figure 12(A)*). The particular trend
807 in *Schmidt et al. (2016)* appears to be due to assumptions of cell size and we provide a more extensive discussion
808 and analysis of that data set in section Additional Considerations of Schmidt et al. Data Set. As a compromise, and
809 in an effort to treat all data equally, we instead scaled all protein abundance values to a data-driven estimate of
810 total protein per cell. Here we used cell size measurements from *Si et al. (2017, 2019)*, and an estimate of total
811 protein content through expected dry mass. Total protein per cell was estimated using available data on total
812 DNA, RNA, and protein from *Basan et al. (2015)*; *Dai et al. (2016)*, which account for the majority of dry mass in the
813 cell. We consider these details in sections Estimation of Cell Size and Surface Area and Estimation of Total Protein
814 Content per Cell that follows.

815 Lastly, in *Figure 13* we show the total proteomic coverage and overlap of proteins quantified across each data

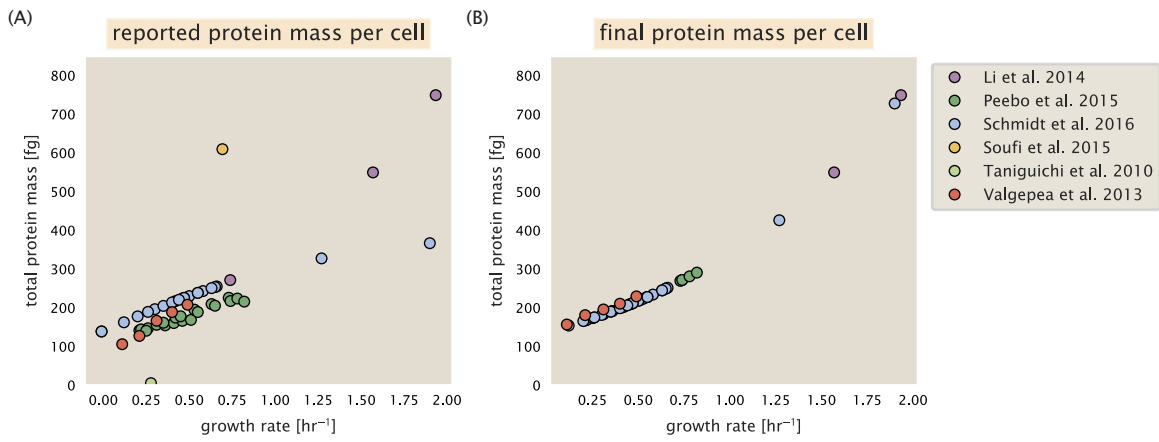


Figure 12. Summary of the growth-rate dependent total protein abundance for each data set. (A) Total protein abundance per cell as original reported in the data sets of *Taniguchi et al. (2010)*; *Valgepea et al. (2013)*; *Li et al. (2014)*; *Soufi et al. (2015)*; *Peebo et al. (2015)*; *Schmidt et al. (2016)*. Note that the data from *Peebo et al. (2015)* only reported protein abundances per unit volume and total protein per cell was found by multiplying these by the growth-rate dependent cell size as determined by *Si et al. (2017)*. (B) Adjusted total protein abundances across the proteomic data sets are summarized. Protein abundances were adjusted so that all data shared a common set of growth-rate dependent total protein per cell and cellular protein concentration following the cell size expectations of *Si et al. (2017)* (see section on Estimation of Cell Size and Surface Area for further details).

set. Here we have used an UpSet diagram (*Lex et al., 2014*) to compare the data. Overall, the overlap in quantified proteins is quite high, with 1157 proteins quantified across all data sets. The sequencing based approach of *Li et al. (2014)* has substantially higher coverage compared to the mass spectrometry data sets (3394 genes versus the 2041 genes quantified in the work of *Schmidt et al. (2016)*). However, in terms of total protein mass, the data from *Li et al. (2014)*; *Schmidt et al. (2016)*; *Peebo et al. (2015)* each quantify roughly equivalent total protein mass. An exception to this is in the data from *Valgepea et al. (2013)*, where we find that the total protein quantified in *Valgepea et al. (2013)* is 90-95 % of the total protein mass (when using the data from *Schmidt et al. (2016)* as a reference).

824 Estimation of Cell Size and Surface Area

825 Since most of the proteomic data sets lack cell size (i.e. volume) measurements, we chose instead to use a common
 826 estimate of size for any analysis requiring cell size or surface area. Since each of the data sets used either K-12
 827 MG1655 or its derivative, BW25113 (from the lab of Barry L. Wanner; the parent strain of the Keio collection
 828 (*Datsenko and Wanner, 2000*; *Baba et al., 2006*)), we fit the MG1655 cell size data from the supplemental material
 829 of *Si et al. (2017, 2019)* using the optimize.curve_fit function from the Scipy python package (*Virtanen et al., 2020*).

830 The average size measurements from each of their experiments are shown in Figure *Figure 14*, with cell length
 831 and width shown in (A) and (B), respectively. The length data was well described by the exponential function 0.5
 832 $e^{1.09 \cdot \lambda} + 1.76 \mu\text{m}$, while the width data was well described by $0.64 e^{0.24 \cdot \lambda} \mu\text{m}$. In order to estimate cell size we take the
 833 cell as a cylinders with two hemispherical ends (*Si et al., 2017*; *Basan et al., 2015*). Specifically, cell size is estimated
 834 from,

$$V = \pi \cdot r^2 \cdot (l - 2r/3), \quad (4)$$

835 where r is half the cell width. A best fit to the data is described by $0.533 e^{1.037 \cdot \lambda} \mu\text{m}^3$. Calculation of the cell surface
 836 area is given by,

$$S = \eta \cdot \pi \left(\frac{\eta \cdot \pi}{4} - \frac{\pi}{12} \right)^{-2/3} V^{2/3}, \quad (5)$$

837 where η is the aspect ratio ($\eta = l/w$) (*Ojkic et al., 2019*).

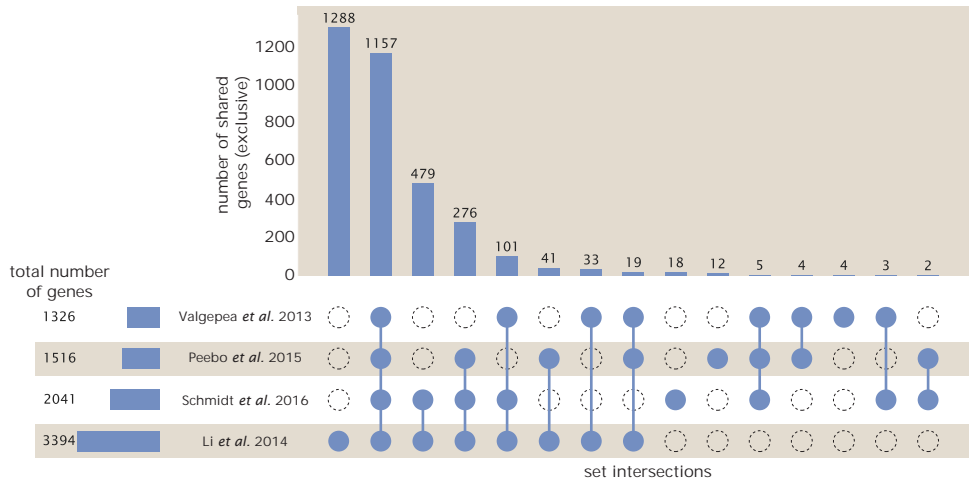


Figure 13. Comparison of proteomic coverage across different data sets. An UpSet diagram (*Lex et al., 2014*) summarizes the total number of protein coding genes whose protein abundance was reported in the data sets of *Valgepea et al. (2013)*; *Li et al. (2014)*; *Schmidt et al. (2016)*; *Peebo et al. (2015)*. The total number of genes reported in each individual data set are noted on the bottom left, while their overlap is summarized in the bar chart. Each column here refers to the intersection of a set of data sets identified by blue circles.

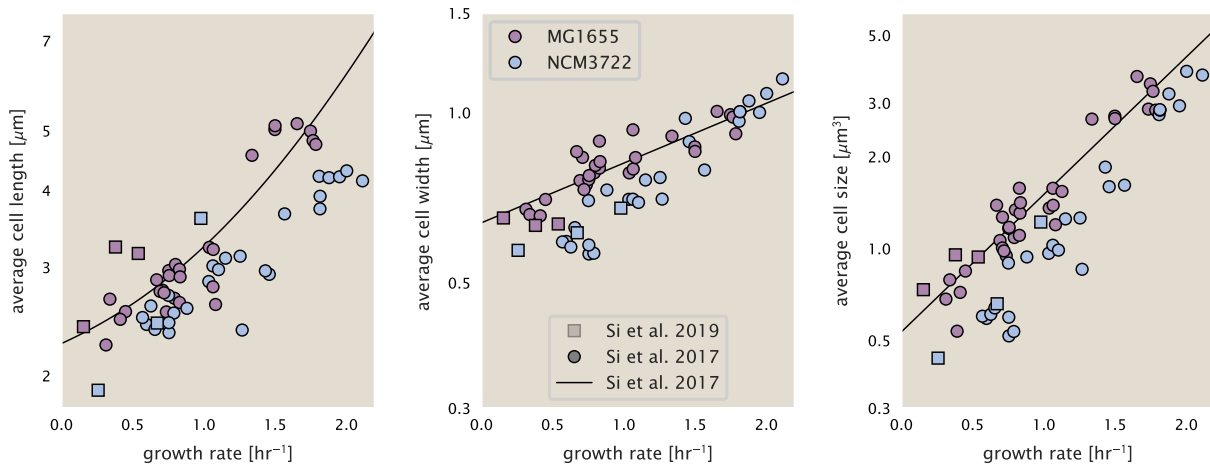


Figure 14. Summary of size measurements from Si et al. 2017, 2019. Cell lengths and widths were measured from cell contours obtained from phase contrast images, and refer to the long and short axis respectively. (A) Cell lengths and (B) cell widths show the mean measurements reported (they report 140-300 images and 5,000-30,000 for each set of samples; which likely means about 1,000-5,000 measurements per mean value reported here since they considered about 6 conditions at a time). Fits were made to the MG1655 strain data; length: $0.5 e^{1.09 \cdot \lambda} + 1.76 \mu\text{m}$, width: $0.64 e^{0.24 \cdot \lambda} \mu\text{m}$. (C) Cell size, V , was calculated as cylinders with two hemispherical ends (Equation 4). The MG1655 strain data gave a best fit of $0.533 e^{1.037 \cdot \lambda} \mu\text{m}^3$.

838 Estimation of Total Protein Content per Cell

839 In order to estimate total protein per cell for a particular growth rate, we begin by estimating the cell size from
840 the fit shown in Figure **Figure 14(C)** ($0.533 e^{1.037 \cdot \lambda} \mu\text{m}^3$). We then estimate the total protein content from the total
841 dry mass of the cell. Here we begin by noting that for almost the entire range of growth rates considered here,
842 protein, DNA, and RNA were reported to account for at least 90 % of the dry mass (**Basan et al. (2015)**). The authors
843 also found that the total dry mass concentration was roughly constant across growth conditions. Under such a
844 scenario, we can calculate the total dry mass concentration for protein, DNA, and RNA, which is given by 1.1 g/ml
845 $\times 30\% \times 90\%$ or about $[M_p] = 300 \text{ fg per fl}$. Multiplying this by our prediction of cell size gives the total dry mass
846 per cell.

847 However, even if dry mass concentration is relatively constant across growth conditions, it is not obvious how
848 protein concentration might vary due to the substantial increase in rRNA at faster growth rates (**Dai et al. (2016)**).
849 This is a well-documented result that arises from an increase in ribosomal abundance at faster growth rates (**Scott**
850 **et al. (2010)**). To proceed therefore rely on experimental measurements of total DNA content per cell that also
851 come from Basan *et al.*, and RNA to protein ratios that were measured in Dai *et al.* (and cover the entire range of
852 growth conditions considered here). These are reproduced in Figure **Figure 15(A)** and (B), respectively.

853 Assuming that the protein, DNA, and RNA account for 90 % of the total dry mass, the protein mass can then de-
854 termined by first subtracting the experimentally measured DNA mass, and then using the experimental estimate
855 of the RNA to protein ratio. The total protein per cell is will be related to the summed RNA and protein mass by,

$$856 M_p = \frac{[M_p + M_{RNA}]}{1 + (RP_{ratio})}. \quad (6)$$

857 (RP_{ratio} refers to the RNA to protein ratio as measured by Dai *et al.*). In Figure **Figure 15(C)** we plot the estimated
858 cellular concentrations for protein, DNA, and RNA from these calculations, and in Figure **Figure 15(D)** we plot their
859 total expected mass per cell. This later quantity is the growth rate-dependent total protein mass that was used to
estimate total protein abundance across all data sets (and summarized in **Figure 12(B)**).

860 Estimating Volume and Number of Amino Acids from Ribosome Copy Number

861 Towards the end of the main text, we examine a coarse-grained model of nutrient-limited growth. A key point
862 in our analysis was to consider how elongation rate r_e and growth rate λ vary with respect to the experimentally
863 observed changes in cell size, total number of peptide bonds per cell N_{pep} , and ribosomal content. In order to
864 do maintain parameters in line with the experimental data, but otherwise allow us to explore the model, we
865 performed a phenomenological fit of N_{pep} and V as a function of the measured ribosomal copy number R . As has
866 been described in the preceding sections of this supplement, we estimate cell volume for each growth condition
867 using the size measurements from **Si et al. (2017, 2019)**, and N_{pep} is approximated by taking the total protein mass
868 and dividing this number by the average mass of an amino acid, 110 Da (BNID: 104877).

869 Given the exponential scaling of V and N_{pep} with growth rate, we performed a linear regression of the log trans-
870 form of these parameters as a function of the log transform of the ribosome copy number. Using optimization
871 by minimization, we estimated the best-fit values of the intercept and slope for each regression. **Figure 16** shows
872 the result of each regression as a dashed line.

873 Additional Considerations of Schmidt *et al.* Data Set

874 While the data set from **Schmidt et al. (2016)** remains a heroic effort that our labs continue to return to as a
875 resource, there were steps taken in their calculation of protein copy number that we felt needed further consider-
876 ation. In particular, the authors made an assumption of constant cellular protein concentration across all growth
877 conditions and used measurements of cell volume that appear inconsistent with an expected exponential scaling
878 of cell size with growth rate that is well-documented in *E. coli* (**Schaechter et al. (1958); Taheri-Araghi et al. (2015);**
879 **Si et al. (2017)**).

880 We begin by looking at their cell volume measurements, which are shown in blue in Figure **Figure 17**. As a
881 comparison, we also plot cell sizes reported in three other recent papers: measurements from Taheri-Araghi *et*
882 *al.* and Si *et al.* come from the lab of Suckjoon Jun, while those from Basan *et al.* come from the lab of Terence
883 Hwa. Each set of measurements used microscopy and cell segmentation to determine the length and width, and

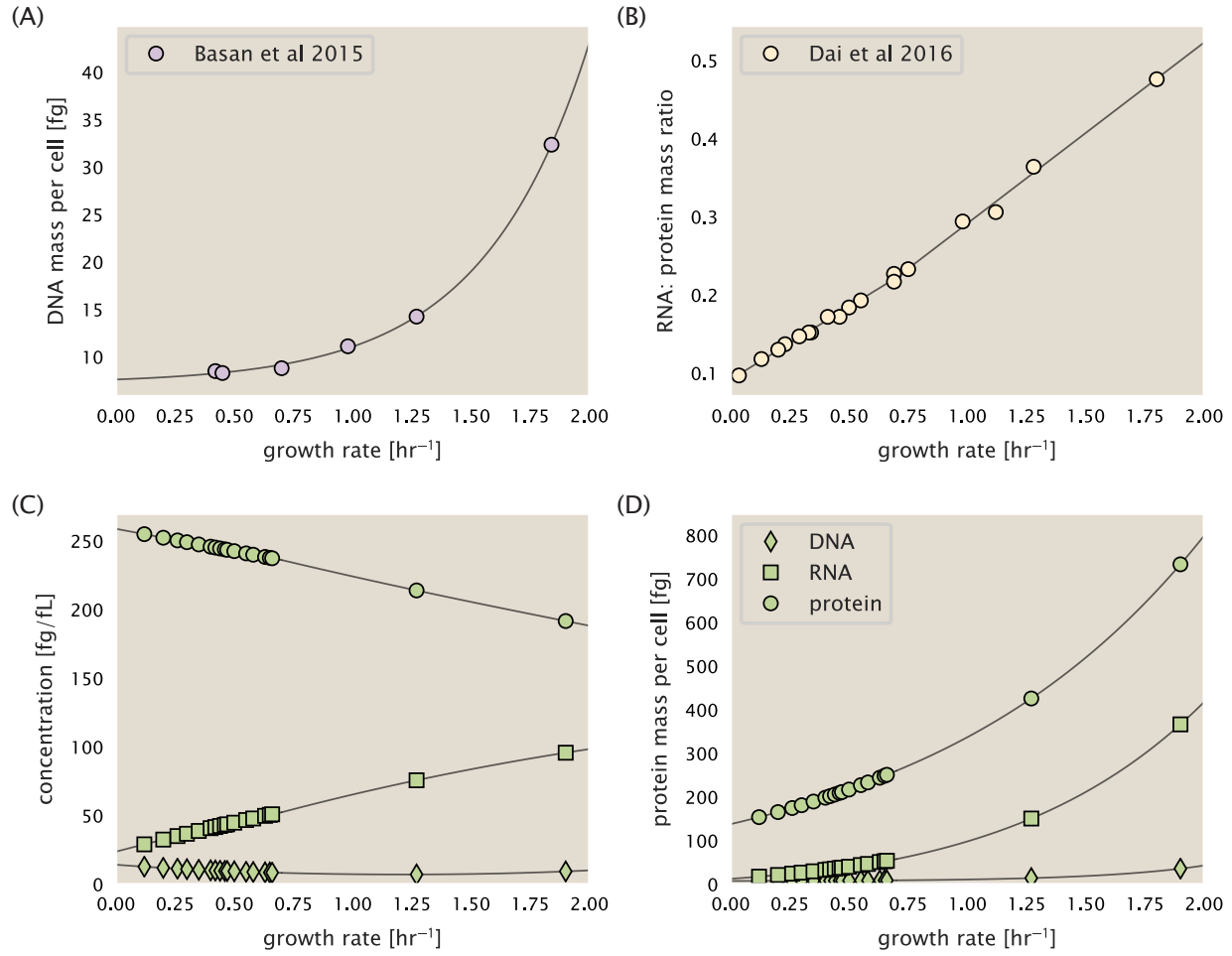


Figure 15. Empirical estimate of cellular protein, DNA, and RNA as a function of growth rate. (A) Measured DNA mass per cell as a function of growth rate, reproduced from Basan *et al.* 2015. The data was fit to an exponential curve (DNA mass in fg per cell is given by $0.42 e^{2.23 \cdot \lambda} + 7.2$ fg per cell, where λ is the growth rate in hr^{-1}). (B) RNA to protein measurements as a function of growth rate. The data was fit to two lines: for growth rates below 0.7 hr^{-1} , the RNA/protein ratio is $0.18 \cdot \lambda + 0.093$, while for growth rates faster than 0.7 hr^{-1} the RNA/protein ratio is given by $0.25 \cdot \lambda + 0.035$. For (A) and (B) cells are grown under varying levels of nutrient limitation, with cells grown in minimal media with different carbon sources for the slowest growth conditions, and rich-defined media for fast growth rates. (C) Predictions of cellular protein, DNA, and RNA concentration. (D) Total cellular mass predicted for protein, DNA, and RNA using the cell size predictions from Si *et al.*. Symbols (diamond: DNA, square: RNA, circle: protein) show estimated values of mass concentration and mass per cell for the specific growth rates in Schmidt *et al.* (2016).

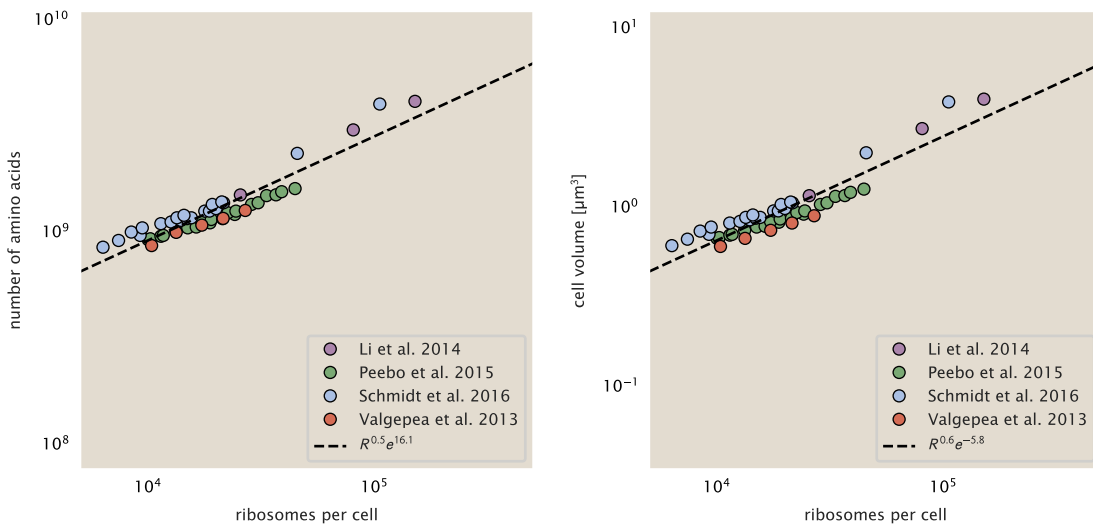


Figure 16. Phenomenological regression of cell volume and number of amino acids per cell as a function of the ribosome copy number. Colored points correspond to the measured value (or calculated value in the case of the cell volume) with colors denoting different data sets. The dashed black line shows the result of the fit, with the functional form of the equation given in the legend with R representing the ribosome copy number.

then calculated cell size by treating the cell as a cylinder with two hemispherical ends, as we considered in the previous section. While there is notable discrepancy between the two research groups, which are both using strain NCM3722, Basan *et al.* found that this came specifically from uncertainty in determining the cell width. This is prone to inaccuracy given the small cell size and optical resolution limits (further described in their supplemental text). Perhaps the more concerning point is that while each of these alternative measurements show an exponential increase in cell size at faster growth rates, the measurements used by Schmidt *et al.* appear to plateau. This resulted in an analogous trend in their final reported total cellular protein per cell as shown in Figure [Figure 18](#) (purple data points), and is in disagreement with other measurements of total protein at these growth rates ([Basan et al., 2015](#)).

Since it is not obvious how measurements of cell size influenced their reported protein abundances, in the following subsections we begin by considering this calculation. We then consider three different approaches to estimate the growth-rate dependent total protein mass to compare with those values reported from [Schmidt et al. \(2016\)](#). The results of this are summarized in [Figure 17\(B\)](#), with the original values from both [Schmidt et al. \(2016\)](#) and [Li et al. \(2014\)](#) shown in [Figure 17\(A\)](#) for reference. For most growth conditions, we find that total protein per cell is still in reasonable agreement. However, for the fastest growth conditions, with glycerol + supplemented amino acids, and LB media, all estimates are substantially higher than those originally reported. This is the main reason why we chose to readjusted protein abundance as shown in [Figure 12\(B\)](#) (with the calculation described in section [Estimation of Total Protein Content per Cell](#)).

Effect of cell volume on reported absolute protein abundances

As noted in section [Experimental Details Behind Proteomic Data](#), the authors calculated proteome-wide protein abundances by first determining absolute abundances of 41 pre-selected proteins, which relied on adding synthetic heavy reference peptides into their protein samples at known abundance. This absolute quantitation was performed in replicate for each growth condition. Separately, the authors also performed a more conventional mass spectrometry measurement for samples from each growth condition, which attempted to maximize the number of quantified proteins but only provided relative abundances based on peptide intensities. Finally, using their 41 proteins with absolute abundances already determined, they then created calibration curves with which to relate their relative intensity to absolute protein abundance for each growth condition. This allowed them to estimate absolute protein abundance for all proteins detected in their proteome-wide data set. Combined with

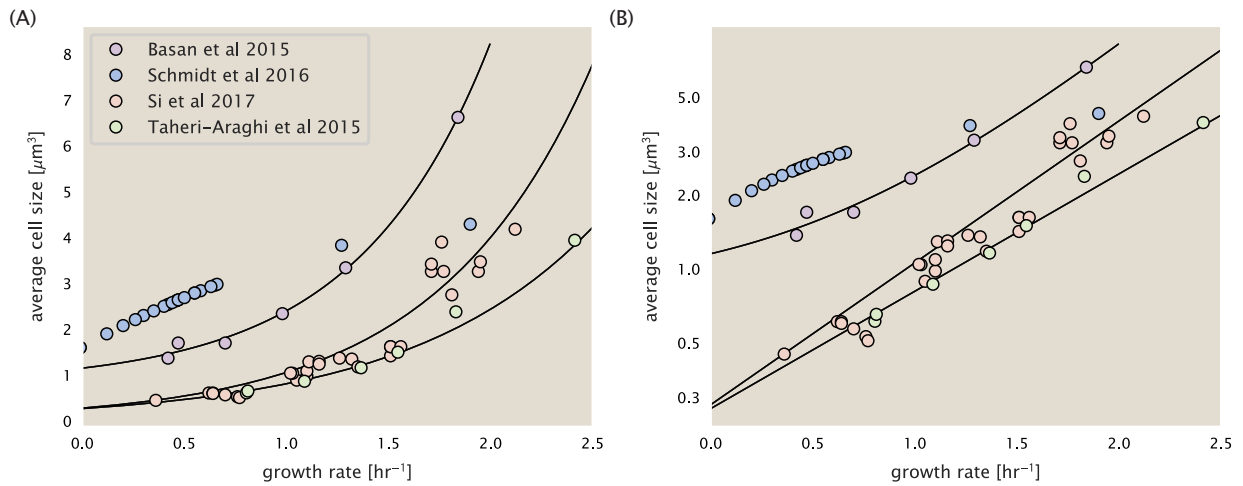


Figure 17. Measurements of cell size as a function of growth rate. (A) Plot of the reported cell sizes from several recent papers. The data in blue come from Volkmer and Heinemann, 2011 ([Volkmer and Heinemann \(2011\)](#)) and were used in the work of Schmidt *et al.*. Data from the lab of Terence Hwa are shown in purple ([Basan *et al.* \(2015\)](#)), while the two data sets shown in green and red come from the lab of Suckjoon Jun ([Taheri-Araghi *et al.* \(2015\); Si *et al.* \(2017\)](#)). (B) Same as in (A) but with the data plotted on a logarithmic y-axis to highlight the exponential scaling that is expected for *E. coli*.

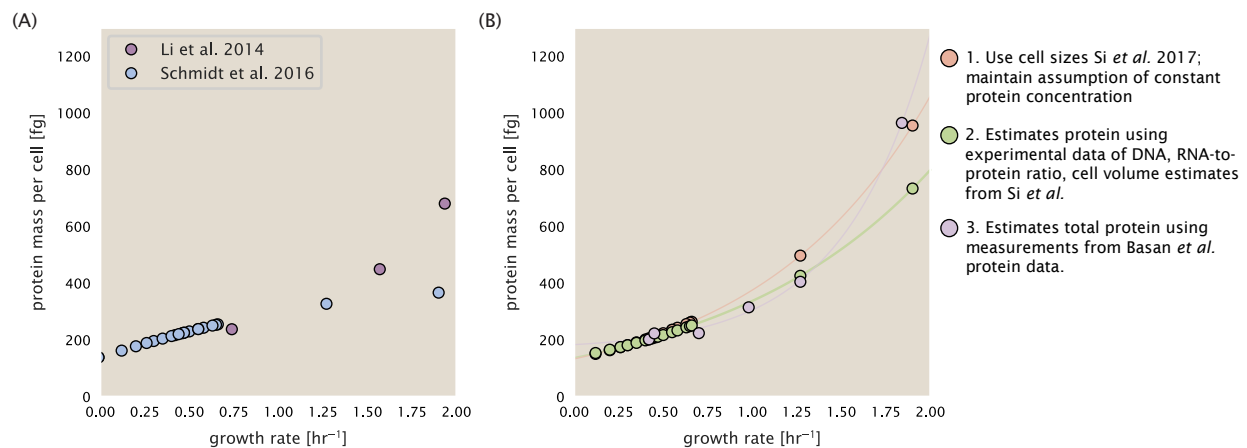


Figure 18. Alternative estimates of total cellular protein for the growth conditions considered in Schmidt *et al.* (A) The original protein mass from Schmidt *et al.* and Li *et al.* are shown in purple and blue, respectively. (B) Three alternative estimates of total protein per cell. 1. *light red*: Rescaling of total protein mass assuming a growth rate independent protein concentration and cell volumes estimated from Si *et al.* 2017. 2. *light green*: Rescaling of total protein mass using estimates of growth rate-dependent protein concentrations and cell volumes estimated from Si *et al.* 2017. Total protein per cell is calculated by assuming a 1.1 g/ml cellular mass density, 30% dry mass, with 90% of the dry mass corresponding to DNA, RNA, and protein ([Basan *et al.*, 2015](#)). See [Estimation of Total Protein Content per Cell](#) for details on calculation. 3. *light purple*: Rescaling of total protein mass using the experimental measurements from Basan *et al.* 2015.

912 their flow cytometry cell counts, they were then able to determine absolute abundance of each protein detected
913 on a per cell basis.

914 While this approach provided absolute abundances, another necessary step to arrive at total cellular protein
915 was to account for any protein loss during their various protein extraction steps. Here the authors attempted
916 to determine total protein separately using a BCA protein assay. In personal communications, it was noted that
917 determining reasonable total protein abundances by BCA across their array of growth conditions was particularly
918 troublesome. Instead, they noted confidence in their total protein measurements for cells grown in M9 minimal
919 media + glucose and used this as a reference point with which to estimate the total protein for all other growth
920 conditions.

921 For cells grown in M9 minimal media + glucose an average total mass of $M_p = 240$ fg per cell was measured.
922 Using their reported cell volume, reported as $V_{orig} = 2.84$ fl, a cellular protein concentration of $[M_p]_{orig} = M_p/V_{orig} =$
923 85 fg/fl. Now, taking the assumption that cellular protein concentration is relatively independent of growth rate,
924 they could then estimate the total protein mass for all other growth conditions from,

$$M_{P_i} = [M_p]_{orig} \cdot V_i \quad (7)$$

925 where M_{P_i} represents the total protein mass per cell and V_i is the cell volume for each growth condition i as mea-
926 sured in Volkmer and Heinemann, 2011. Here the thinking is that the values of M_{P_i} reflects the total cellular protein
927 for growth condition i , where any discrepancy from their absolute abundance is assumed to be due to
928 protein loss during sample preparation. The protein abundances from their absolute abundance measurements
929 noted above were therefore scaled to their estimates and are shown in Figure **Figure 18** (purple data points).

930 If we instead consider the cell volumes predicted in the work of Si *et al.*, we again need to take growth in M9
931 minimal media + glucose as a reference with known total mass, but we can follow a similar approach to estimate
932 total protein mass for all other growth conditions. Letting $V_{Si_glu} = 0.6$ fl be the predicted cell volume, the cellular
933 protein concentration becomes $[M_p]_{Si} = M_p/V_{Si_glu} = 400$ fg/fl. The new total protein mass per cell can then be
934 calculated from,

$$M'_{P_i} = [M_p]_{Si} \cdot V_{Si_i} \quad (8)$$

935 where M'_{P_i} is the new protein mass prediction, and V_{Si_i} refers to the new volume prediction for each condition i ,
936 These are shown as red data points in Figure **Figure 18(B)**.

937 Relaxing assumption of constant protein concentration across growth conditions

938 We next relax the assumption that cellular protein concentration is constant and instead, attempt to estimate it
939 using experimental data. Here we use the estimation of total protein mass per cell detailed in section **Estimation**
940 of Total Protein Content per Cell for all data points in the **Schmidt *et al.* (2016)** data set. The green data points in
941 **Figure 18(B)** show this prediction, and this represents the approach used to estimate total protein per cell for all
942 data sets.

943 Comparison with total protein measurements from Basan *et al.* 2015.

944 One of the challenges in our estimates in the preceding sections is the need to estimate protein concentration
945 and cell volumes. These are inherently difficult to accurately due to the small size of *E. coli*. Indeed, for all
946 the additional measurements of cell volume included in Figure **Figure 17**, no measurements were performed for
947 cells growing at rates below 0.5 hr^{-1} . It therefore remains to be determined whether our extrapolated cell volume
948 estimates are appropriate, with the possibility that the logarithmic scaling of cell size might break down for slower
949 growth.

950 In our last approach we therefore attempt to estimate total protein using experimental data that required no
951 estimates of concentration or cell volume. Specifically, in the work of Basan *et al.*, the authors measured total
952 protein per cell for a broad range of growth rates (reproduced in Figure **Figure 19**). These were determined by
953 first measuring bulk protein from cell lysate, measured by the colorimetric Biuret method (**You *et al.* (2013)**), and
954 then abundance per cell was calculated from cell counts from either plating cells or a Coulter counter. While it
955 is unclear why Schmidt *et al.* was unable to take a similar approach, the results from Basan *et al* appear more

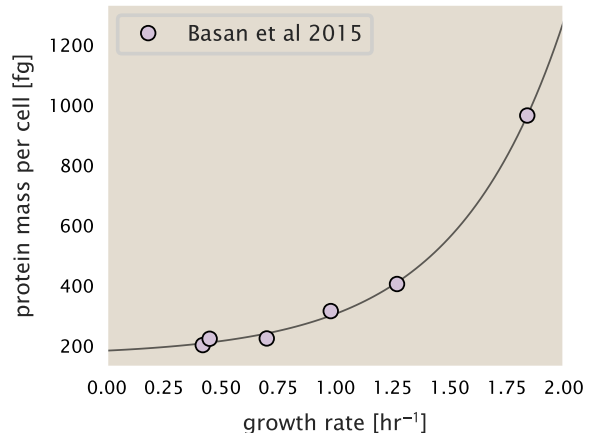


Figure 19. Total cellular protein reported in Basan et al. 2015. Measured protein mass as a function of growth rate as reproduced from Basan *et al.* 2015, with cells grown under different levels of nutrient limitation. The data was fit to an exponential curve where protein mass in fg per cell is given by $14.65 e^{2.180 \cdot \lambda} + 172$ fg per cell, where λ is the growth rate in hr^{-1} .

956 consistent with our expectation that cell mass will increase exponentially with faster growth rates. In addition,
 957 although they do not consider growth rates below about $0.5\ hr^{-1}$, it is interesting to note that the protein mass
 958 per cell appears to plateau to a minimum value at slow growth. In contrast, our estimates using cell volume so far
 959 have predicted that total protein mass should continue to decrease slightly for slower growing cells. By fitting this
 960 data to an exponential function dependent on growth rate, we could then estimate the total protein per cell for
 961 each growth condition considered by *Schmidt et al. (2016)*. These are plotted as red data points in *Figure 18(B)*.

962 Calculation of Complex Abundance

963 All protein data quantified the abundance of individual proteins per cell. However, this work requires estimates
 964 on the abundance of individual protein *complexes*, rather than the copy number of individual proteins. In this
 965 section, we outline the approach we used to annotate proteins as being part of a macromolecular complex and
 966 how we computed their absolute abundances per cell.

967 Protein complexes, and proteins individually, often have a variety of names, both longform and shorthand. As
 968 individual proteins can have a variety of different synonyms, we sought to ensure that each protein annotated
 969 in the data sets used the same synonym. To do use, we relied heavily on the EcoCyc Genomic Database (*Keseler*
 970 *et al., 2017*). Each protein in available data sets included an annotation of one of the gene name synonyms as
 971 well as an accession ID – either a UniProt or Blattner “b-number”. We programmatically matched up individual
 972 accession IDs between the proteins in different data sets. In cases where accession IDs matched but the gene
 973 names were different, we manually verified that the gene product was the same between the datasets and chose
 974 a single synonym. All code used in the data cleaning and unification procedures can be found on the associated
 975 [GitHub repository] (DOI:XXX) associated with this paper as well as on the associated [paper website](#).

976 With each protein conforming to a single identification scheme, we then needed to identify the molecular
 977 complexes each protein was a member of. Additionally, we needed to identify how many copies of each protein
 978 were present in each complex (i.e. the subunit copy number) and compute the estimated abundance complex
 979 that accounted for fluctuations in subunit stoichiometry. To map proteins to complexes, we accessed the EcoCyc
 980 *E. coli* database *Keseler et al. (2017)* using PathwayTools version 23.0 *Karp et al. (2019)*. With a license for PathWay
 981 Tools, we mapped each unique protein to its annotated complexes via the BioCyc Python package. As we mapped
 982 each protein with *all* of its complex annotations, there was redundancy in the dataset. For example, ribosomal
 983 protein L20 (RplT) is annotated to be a component of the 50S ribosome (EcoCyc complex CPLX-03962) as well as a
 984 component of the mature 70S ribosome (EcoCyc complex CPLX-03964).

985 In addition to the annotated complex, we collected information on the stoichiometry of each macromolecular
 986 complex. For a complex with N_{subunits} protein species, for each protein subunit i we first calculate the number of

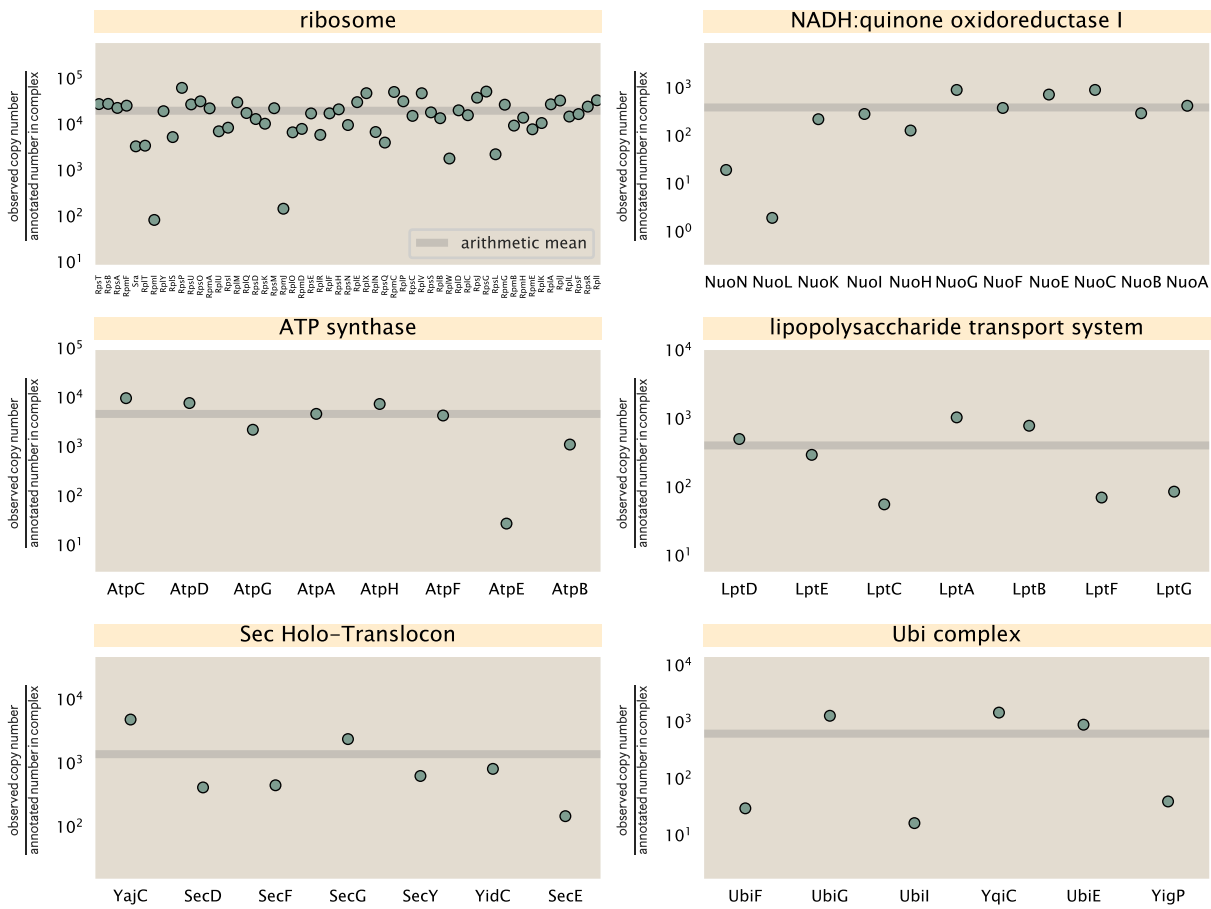


Figure 20. Calculation of the mean complex abundance from measurements of single subunits. Six of the largest complexes (by number of subunits) in *E. coli*. Points correspond to the maximum number of complexes that can be formed given measurement of that individual protein. Solid grey line corresponds to the arithmetic mean across all subunits. These data correspond to measurements from Schmidt et al. (2016) in a glucose-supplemented minimal growth medium.

complexes that could be formed given the measured protein copy numbers per cell,

$$N_{\text{complex}}(\text{subunit } i) = \frac{P_{\text{subunit } i}^{(\text{measured})}}{m_{\text{subunit } i}}. \quad (9)$$

Here, $P_{\text{subunit } i}^{(\text{measured})}$ refers to the measured protein copy number of species i , and m refers to the number of monomers present for that protein in the complex. For example, the 70S mature ribosome complex has 55 protein components, all of which are present in a single copy except L4 (RplL), which is present in 4 copies ($m = 4$). For each ribosomal protein, we then calculate the maximum number of complexes that could be formed using Equation 9. This example, along with example from 5 other macromolecular complexes, can be seen in Figure 20.

It is important to note that measurement noise, efficiency of protein extraction, and differences in protein stability will mean that the precise value of each calculation will be different for each component of a given complex. Thus, to report the total complex abundance, we use the arithmetic mean of across all subunits in the complex,

$$\langle N_{\text{complex}} \rangle = \frac{1}{N_{\text{subunits}}} \sum_i^{N_{\text{subunits}}} \frac{P_i^{(\text{measured})}}{m_{\text{subunit } i}}. \quad (10)$$

in Figure 20, we show this mean value as a grey line for a variety of different complexes. Additionally, we have built an interactive figure accessible on the [paper website](#) where the validity of this approach can be examined for any complex with more than two subunits (thus, excluding monomers and dimers).

999 Extending Estimates to a Continuum of Growth Rates

1000 In the main text, we considered a standard stopwatch of 5000 s to estimate the abundance of the various protein
1001 complexes considered. In addition to point estimates, we also showed the estimate as a function of growth rate
1002 as transparent grey curves. In this section, we elaborate on this continuum estimate, giving examples of estimates
1003 that scale with either cell volume, cell surface area, or number of origins of replication.

1004 Estimation of the total cell mass

1005 For many of the processes estimated in the main text we relied on a cellular dry mass of ≈ 300 fg from which we
1006 computed elemental and protein fractions using knowledge of fractional composition of the dry mass. At modest
1007 growth rates, such as the 5000 s doubling time used in the main text, this is a reasonable number to use as the
1008 typical cell mass is ≈ 1 pg and *E. coli* cells can approximated as 70% water by volume. However, as we have shown
1009 in the preceding sections, the cell size is highly dependent on the growth rate. This means that a dry mass of 300
1010 fg cannot be used reliably across all growth rates.

1011 Rather, using the phenomenological description of cell volume scaling exponentially with growth rate, and
1012 using a rule-of-thumb of a cell buoyant density of ≈ 1.1 pg / fL (BNID: 103875), we can calculate the cell dry mass
1013 across a range of physiological growth rates as

$$m_{\text{cell}} \approx \rho V(\lambda) \approx \rho a e^{\lambda * b} \quad (11)$$

1014 where a and b are constants with units of μm^3 and hr, respectively. The value of these constants can be estimated
1015 from the careful volume measurements performed by *Si et al. (2017,?)*, as considered in Appendix Estimation of
1016 Cell Size and Surface Area earlier.

1017 Complex Abundance Scaling With Cell Volume

1018 Several of the estimates performed in the main text are implicitly dependent on the cell volume. This includes
1019 processes such as ATP utilization and, most prominently, the transport of nutrients, whose demand will be pro-
1020 portional to the volume of the cell. Of the latter, we estimated the number of transporters that would be needed
1021 to shuttle enough carbon, phosphorus, and sulfur across the membrane to build new cell mass. To do so, we
1022 used elemental composition measurements combined with a 300 fg cell dry mass to make the point estimate. As
1023 we now have a means to estimate the total cell mass as a function of volume, we can generalize these estimates
1024 across growth rates.

1025 Rather than discussing the particular details of each transport system, we will derive this scaling expression in
1026 very general terms. Consider that we wish to estimate the number of transporters for some substance X , which
1027 has been measured to be made up some fraction of the dry mass, θ_X . If we assume that, irrespective of growth
1028 rate, the cell dry mass is relatively constant (*Basan et al., 2015*) and $\approx 30\%$ of the total cell mass, we can state that
1029 the total mass of substance X as a function of growth rate is

$$m_X \approx 0.3 \times \rho V(\lambda) \theta_X, \quad (12)$$

1030 where we have used $\rho V(\lambda)$ as an estimate of the total cell mass, defined in *Equation 11*. To convert this to the
1031 number of units N_X of substance X in the cell, we can use the formula weight w_X of a single unit of X in conjunction
1032 with *Equation 12*,

$$N_X \approx \frac{m_X}{w_X}. \quad (13)$$

1033 To estimate the number of transporters needed, we make the approximation that loss of units of X via diffusion
1034 through porins or due to the permeability of the membrane is negligible and that a single transporter complex
1035 can transport substance X at a rate r_X . As this rate r_X is in units of X per time per transporter, we must provide
1036 a time window over which the transport process can occur. This is related to the cell doubling time τ , which can
1037 be calculated from the the growth rate λ as $\tau = \log(2)/\lambda$. Putting everything together, we arrive at a generalized
1038 transport scaling relation of

$$N_{\text{transporters}}(\lambda) = \frac{0.3 \times \rho V(\lambda) \theta_X}{w_X r_X \tau}. \quad (14)$$

1039 This function is used to draw the continuum estimates for the number of transporters seen in Figures 2 and
 1040 3 as transparent grey curves. Occasionally, this continuum scaling relationship will not precisely agree with the
 1041 point estimate outlined in the main text. This is due to the choice of ≈ 300 fg total dry mass per cell for the point
 1042 estimate, whereas we considered more precise values of cell mass in the continuum estimate. We note, however,
 1043 that both this scaling relation and the point estimates are meant to describe the order-of-magnitude observed,
 1044 and not the predict the exact values of the abundances.

1045 **Equation 14** is a very general relation for processes where the cell volume is the "natural variable" of the
 1046 problem. This means that, as the cell increases in volume, the requirements for substance X also scale with
 1047 volume rather than scaling with surface area, for example. So long as the rate of the process, the fraction of the
 1048 dry mass attributable to the substance, and the formula mass of the substance is known, **Equation 14** can be used
 1049 to compute the number of complexes needed. For example, to compute the number of ATP synthases per cell,
 1050 **Equation 14** can be slightly modified to the form

$$N_{\text{ATP synthases}}(\lambda) = \frac{0.3 \times \rho V(\lambda) \theta_{\text{protein}} N_{\text{ATP}}}{w_{AA} r_{\text{ATP}} \tau}, \quad (15)$$

1051 where we have included the term N_{ATP} to account for the number of ATP equivalents needed per amino acid for
 1052 translation (≈ 4 , BNID: 114971), and w_{AA} is the average mass of an amino acid. The grey curves in Figure 4 o the
 1053 main text were made using this type of expression.

1054 A Relation for Complex Abundance Scaling With Surface Area

1055 In our estimation for the number of complexes needed for lipid synthesis and peptidoglycan maturation, we used
 1056 a particular estimate for the cell surface area ($\approx 5 \mu\text{m}$, BNID: 101792) and the fraction of dry mass attributable to
 1057 peptidoglycan ($\approx 3\%$, BNID: 101936). Both of these values come from glucose-fed *E. coli* in balance growth. As we
 1058 are interested in describing the scaling as a function of the growth rate, we must also consider how these values
 1059 scale with cell surface area, which is the natural variable for these types of processes. In the coming paragraphs,
 1060 we highlight how we incorporate a condition-dependent surface area into our calculation of the number of lipids
 1061 and murein monomers that need to be synthesized and crosslinked, respectively.

1062 Number of Lipids

1063 To compute the number of lipids as a function of growth rate, we make the assumption that some features, such as
 1064 the surface area of a single lipid ($A_{\text{lipid}} \approx 0.5 \text{ nm}^2$, BNID: 106993) and the total fraction of the membrane composed
 1065 of lipids ($\approx 40\%$, BNID: 100078) are independent of the growth rate. Using these approximations combined with
 1066 **Equation 5**, and recognizing that each membrane is composed of two leaflets, we can compute the number of
 1067 lipids as a function of growth rate as

$$N_{\text{lipids}}(\lambda) \approx \frac{4 \text{ leaflets} \times 0.4 \times \eta \pi \left(\frac{\eta \pi}{4} - \frac{\pi}{12} \right)^{-2/3} V(\lambda)^{2/3}}{A_{\text{lipid}}} \quad (16)$$

1068 where η is the length-to-width aspect ratio and V is the cell volume.

1069 Number of Murein Monomers

1070 In calculation of the number of transpeptidases needed for maturation of the peptidoglycan, we used an empirical
 1071 measurement that $\approx 3\%$ of the dry mass is attributable to peptidoglycan and that a single murien monomer is
 1072 $m_{\text{murein}} \approx 1000 \text{ Da}$. While the latter is independent of growth rate, the former is not. As the peptidoglycan exists as
 1073 a thin shell with a width of $w \approx 10 \text{ nm}$ encapsulating the cell, one would expect the number of murein monomers
 1074 scales with the surface area of this shell. In a similar spirit to our calculation of the number of lipids, the total
 1075 number of murein monomers as a function of growth rate can be calculated as

$$N_{\text{murein monomers}}(\lambda) \approx \frac{\rho_{\text{pg}} w \eta \pi \left(\frac{\eta \pi}{4} - \frac{\pi}{12} \right)^{-2/3} V(\lambda)^{2/3}}{m_{\text{murein}}}, \quad (17)$$

1076 where ρ_{pg} is the density of peptidoglycan.

1077 **Complex Abundance Scaling With Number of Origins, and rRNA Synthesis**

1078 While the majority of our estimates hinge on the total cell volume or surface area, processes related to the central
1079 dogma, namely DNA replication and synthesis of rRNA, depend on the number of chromosomes present in the
1080 cell. As discussed in the main text, the ability of *E. coli* to parallelize the replication of its chromosome by having
1081 multiple active origins of replication is critical to synthesize enough rRNA, especially at fast growth rates. Derived
1082 in *Si et al. (2017)* and reproduced in the main text and Appendix Estimation of $\langle \#ori \rangle / \langle \#ter \rangle$ and $\langle \#ori \rangle$ below, the
1083 average number of origins of replication at a given growth rate can be calculated as

$$\langle \#ori \rangle \approx 2^{t_{\text{cyc}} \lambda / \ln 2} \quad (18)$$

1084 where t_{cyc} is the total time of replication and division. We can make the approximation that $t_{\text{cyc}} \approx 70$ min, which is
1085 the time it takes two replisomes to copy an entire chromosome.

1086 In the case of rRNA synthesis, the majority of the rRNA operons are surrounding the origin of replication. Thus,
1087 at a given growth rate λ , the average dosage of rRNA operons per cell D_{rRNA} is

$$D_{\text{rRNA}}(\lambda) \approx N_{\text{rRNA operons}} \times 2^{t_{\text{cyc}} \lambda / \ln 2}. \quad (19)$$

1088 This makes the approximation that *all* rRNA operons are localized around the origin. In reality, the operons
1089 are some distance away from the origin, making **Equation 19** an approximation (*Dennis et al., 2004*).

1090 In the main text, we stated that at a growth rate of 0.5 hr^{-1} , there is ≈ 1 chromosome per cell. While a fair
1091 approximation, **Equation 18** illustrates that is not precisely true, even at slow growth rates. In estimating the
1092 number of RNA polymerases as a function of growth rate, we consider that regardless of the number of rRNA
1093 operons, they are all sufficiently loaded with RNA polymerase such that each operon produces one rRNA per
1094 second. Thus, the total number of RNA polymerase as a function of the growth rate can be calculated as

$$N_{\text{RNA polymerase}}(\lambda) \approx L_{\text{operon}} D_{\text{rRNA}} \rho_{\text{RNA polymerase}}, \quad (20)$$

1095 where L_{operon} is the total length of an rRNA operon (≈ 4500 bp) and $\rho_{\text{RNA polymerase}}$ is packing density of RNA poly-
1096 merase on a given operon, taken to be 1 RNA polymerase per 80 nucleotides.

1097 **Calculation of active ribosomal fraction.**

1098 In the main text we used the active ribosomal fraction f_a that was reported in the work of *Dai et al. (2016)* to
1099 estimate the active ribosomal mass fraction $\Phi_R \times f_a$ across growth conditions. We lacked any specific model to
1100 consider how f_a should vary with growth rate, and instead find that the data is well-approximated by fitting to an
1101 exponential curve ($f_a = -0.889 e^{4.6 \cdot \lambda} + 0.922$; dashed line in inset of **Figure 9(C)**). We use this function to estimate f_a
1102 for each of the data points shown in **Figure 9(C)**.

1103 **Estimation of $\langle \#ori \rangle / \langle \#ter \rangle$ and $\langle \#ori \rangle$.**

1104 *E. coli* shows robust scaling of cell size with the average the number of origins $\langle \#ori \rangle$ per cell (*Si et al., 2017*). Since
1105 protein makes up a majority of the cell's dry mass, the change in cell size is also a reflection of the changes in
1106 proteomic composition and total abundance across growth conditions. Given the potential constraints on rRNA
1107 synthesis and changes in ribosomal copy number with $\langle \#ori \rangle$, it becomes important to also consider how pro-
1108 tein copy numbers vary with the state of chromosomal replication. This is particularly true when trying to make
1109 sense of the changes in ribosomal fraction and growth-rate dependent changes in proteomic composition at a
1110 mechanistic level. As considered in the main text, it is becoming increasingly apparent that regulation through
1111 the secondary messengers (p)ppGpp may act to limit DNA replication and also reduce ribosomal activity in poorer
1112 nutrient conditions. In this context, both $\langle \#ori \rangle$, as well as the $\langle \#ori \rangle / \langle \#ter \rangle$ ratio become important parameters
1113 to consider and keep tract of. An increase in $\langle \#ori \rangle / \langle \#ter \rangle$ ratio in particular, causes a relatively higher gene
1114 dosage in rRNA and r-protein genes due to skew in genes near the origin, where the majority of these are located

1115 In the main text we estimated the change in $\langle \#ori \rangle$ with growth rate using the nutrient-limited wild-type cell
1116 data from *Si et al. (2017)*. We consider their measurements of DNA replication time (t_c , 'C' period of cell division),
1117 total cell cycle time (t_{cyc} , 'C' + 'D' period of cell division), and doubling time τ from wild-type *E. coli* growing across
1118 a range of growth conditions. Here we show how we estimate this parameter, as well as the $\langle \#ori \rangle / \langle \#ter \rangle$ ratio

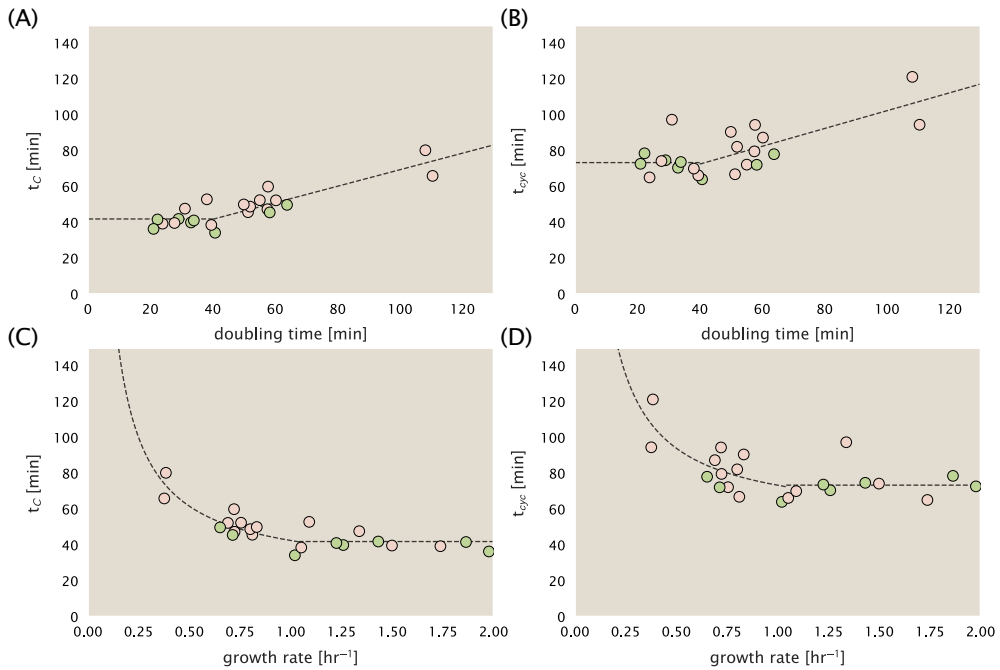


Figure 21. Estimation of $\langle \#ori \rangle / \langle \# ter \rangle$ and $\langle \#ori \rangle$ using data from Si et al. (2017). (A) and (B) plot the reported t_C and t_{cyc} as a function of cell doubling time τ , respectively. The dashed lines show a piecewise fit to the data. For short doubling times (rich media), t_C and t_{cyc} are assumed constant ($t_C = 42$ minutes, $t_{cyc} = 73$ minutes). At the transition, taken to occur at 40 minutes, the dashed line corresponds to an assumed proportional increase in each parameter as a function of the doubling time ($t_C = 0.46\tau + 23.3$ minutes, $t_{cyc} = 0.50\tau + 52.7$ minutes). (C) and (D) plot the same data as in (A) and (B), but as a function of growth rate, given by $\lambda = \ln(2)/\tau$.

from their data. We begin by considering $\langle \#ori \rangle$. If the cell cycle time takes longer than the time of cell division, the cell will need to initiate DNA replication more often than its rate of division, $2^{\lambda t} = 2^{\ln(2)\cdot t/\tau}$ to maintain steady state growth. Cells will need to do this in proportion to the ratio $\lambda_{cyc}/\lambda = t_{cyc}/\tau$, and the number of origins per cell (on average) is then given by $2^{t_{cyc}/\tau}$. The average number of termini will in contrast depend on the lag time between DNA replication and cell division, t_D , with $\langle \#ori \rangle / \langle \# ter \rangle$ ratio = $2^{t_{cyc}/\tau - t_D/\tau} = 2^{t_C/\tau}$.

In Figure 21(A) and (B) we plot the measured t_C and t_{cyc} values versus the doubling time from Si et al. (2017). The authors estimated t_C by marker frequency analysis using qPCR, while $t_{cyc} = t_C + t_D$ were inferred from t_C and τ . In the plots we see that both t_C and t_{cyc} reach a minimum at around 40 and 75 minutes, respectively. For a C period of 40 minutes, this would correspond to a maximum rate of elongation of about 1,000 bp/sec. Since we lacked a specific model to describe how each of these parameters vary with growth condition, we assumed that they were linearly dependent on the doubling time. For each parameter, t_C and t_{cyc} , we split them up into two domains corresponding to poorer nutrient conditions and rich nutrient conditions (cut off at $\tau \approx 40$ minutes where chromosomal replication becomes nearly constant). The fit lines are shown as solid black lines. In Figure 21(C) and (D) we also show t_C and t_{cyc} as a function of growth rate λ along with our piecewise linear fits, which match the plots in the main text.

References

- 1134 Aidelberg, G., Towbin, B. D., Rothschild, D., Dekel, E., Bren, A., and Alon, U. (2014). Hierarchy of non-glucose sugars in *Escherichia*
1135 *coli*. *BMC Systems Biology*, 8(1):133.
- 1136
- 1137 Antonenko, Y. N., Pohl, P., and Denisov, G. A. (1997). Permeation of ammonia across bilayer lipid membranes studied by ammonium ion selective microelectrodes. *Biophysical Journal*, 72(5):2187–2195.
- 1138
- 1139 Ashburner, M., Ball, C. A., Blake, J. A., Botstein, D., Butler, H., Cherry, J. M., Davis, A. P., Dolinski, K., Dwight, S. S., Eppig, J. T., Harris,
1140 M. A., Hill, D. P., Issel-Tarver, L., Kasarskis, A., Lewis, S., Matese, J. C., Richardson, J. E., Ringwald, M., Rubin, G. M., and Sherlock,
1141 G. (2000). Gene Ontology: tool for the unification of biology. *Nature Genetics*, 25(1):25–29.
- 1142 Ason, B., Bertram, J. G., Hingorani, M. M., Beechem, J. M., O'Donnell, M., Goodman, M. F., and Bloom, L. B. (2000). A Model
1143 for *Escherichia coli* DNA Polymerase III Holoenzyme Assembly at Primer/Template Ends: DNA Triggers A Change In Binding
1144 Specificity of the γ Complex Clamp Loader. *Journal of Biological Chemistry*, 275(4):3006–3015.
- 1145 Assentoft, M., Kaptan, S., Schneider, H.-P., Deitmer, J. W., de Groot, B. L., and MacAulay, N. (2016). Aquaporin 4 as a NH₃ Channel.
1146 *Journal of Biological Chemistry*, 291(36):19184–19195.
- 1147 Baba, T., Ara, T., Hasegawa, M., Takai, Y., Okumura, Y., Baba, M., Datsenko, K. A., Tomita, M., Wanner, B. L., and Mori, H. (2006).
1148 Construction of *Escherichia coli*K-12 in-frame, single-gene knockout mutants: the Keio collection. *Molecular Systems Biology*,
1149 2(1):2460.
- 1150 Basan, M., Zhu, M., Dai, X., Warren, M., Sévin, D., Wang, Y.-P., and Hwa, T. (2015). Inflating bacterial cells by increased protein
1151 synthesis. *Molecular Systems Biology*, 11(10):836.
- 1152 Bauer, S. and Ziv, E. (1976). Dense growth of aerobic bacteria in a bench-scale fermentor. *Biotechnology and Bioengineering*,
1153 18(1):81–94. _eprint: <https://onlinelibrary.wiley.com/doi/pdf/10.1002/bit.260180107>.
- 1154 Belliveau, N. M., Barnes, S. L., Ireland, W. T., Jones, D. L., Sweredoski, M. J., Moradian, A., Hess, S., Kinney, J. B., and Phillips, R.
1155 (2018). Systematic approach for dissecting the molecular mechanisms of transcriptional regulation in bacteria. *Proceedings
1156 of the National Academy of Sciences*, 115(21):E4796–E4805.
- 1157 Bremer, H. and Dennis, P. P. (2008). Modulation of Chemical Composition and Other Parameters of the Cell at Different Exponential Growth Rates. *EcoSal Plus*, 3(1).
- 1158
- 1159 Browning, D. F. and Busby, S. J. W. (2016). Local and global regulation of transcription initiation in bacteria. *Nature Reviews
1160 Microbiology*, 14(10):638–650.
- 1161 Büke, F., Grilli, J., Lagomarsino, M. C., Bokinsky, G., and Tans, S. (2020). ppGpp is a bacterial cell size regulator. *bioRxiv*,
1162 266:2020.06.16.154187.
- 1163 Catherwood, A. C., Lloyd, A. J., Tod, J. A., Chauhan, S., Slade, S. E., Walkowiak, G. P., Galley, N. F., Punekar, A. S., Smart, K., Rea, D.,
1164 Evans, N. D., Chappell, M. J., Roper, D. I., and Dowson, C. G. (2020). Substrate and Stereochemical Control of Peptidoglycan
1165 Cross-Linking by Transpeptidation by *Escherichia coli* PBP1B. *Journal of the American Chemical Society*, 142(11):5034–5048.
- 1166 Cox, G. B., Newton, N. A., Gibson, F., Snoswell, A. M., and Hamilton, J. A. (1970). The function of ubiquinone in *Escherichia coli*.
1167 *Biochemical Journal*, 117(3):551–562.
- 1168 Dai, X., Zhu, M., Warren, M., Balakrishnan, R., Okano, H., Williamson, J. R., Fredrick, K., and Hwa, T. (2018). Slowdown of Translational Elongation in *Escherichia coli* under Hyperosmotic Stress. - PubMed - NCBI. *mBio*, 9(1):281.
- 1169
- 1170 Dai, X., Zhu, M., Warren, M., Balakrishnan, R., Patsalo, V., Okano, H., Williamson, J. R., Fredrick, K., Wang, Y.-P., and Hwa, T.
1171 (2016). Reduction of translating ribosomes enables *Escherichia coli* to maintain elongation rates during slow growth. *Nature
1172 Microbiology*, 2(2):16231.
- 1173 Datsenko, K. A. and Wanner, B. L. (2000). One-step inactivation of chromosomal genes in *Escherichia coli* K-12 using PCR products.
1174 *Proceedings of the National Academy of Sciences*, 97(12):6640–6645.
- 1175 Dennis, P. P., Ehrenberg, M., and Bremer, H. (2004). Control of rRNA Synthesis in *Escherichia coli*: a Systems Biology Approach.
1176 *Microbiology and Molecular Biology Reviews*, 68(4):639–668.
- 1177 Dill, K. A., Ghosh, K., and Schmit, J. D. (2011). Physical limits of cells and proteomes. *Proceedings of the National Academy of
1178 Sciences*, 108(44):17876–17882.
- 1179 Erickson, D. W., Schink, S. J., Patsalo, V., Williamson, J. R., Gerland, U., and Hwa, T. (2017). A global resource allocation strategy
1180 governs growth transition kinetics of *Escherichia coli*. *Nature*, 551(7678):119–123.

- 1181 Escalante, A., Salinas Cervantes, A., Gosset, G., and Bolívar, F. (2012). Current knowledge of the *Escherichia coli* phosphoenolpyruvate-carbohydrate phosphotransferase system: Peculiarities of regulation and impact on growth and product formation. *Applied Microbiology and Biotechnology*, 94(6):1483–1494.
- 1184 Fernández-Coll, L., Maciąg-Dorszynska, M., Tailor, K., Vadia, S., Levin, P. A., Szalewska-Palasz, A., Cashel, M., and Dunny, G. M. (2020). The Absence of (p)ppGpp Renders Initiation of *Escherichia coli* Chromosomal DNA Synthesis Independent of Growth Rates. *mBio*, 11(2):45.
- 1187 Fijalkowska, I. J., Schaaper, R. M., and Jonczyk, P. (2012). DNA replication fidelity in *Escherichia coli*: A multi-DNA polymerase affair. *FEMS Microbiology Reviews*, 36(6):1105–1121.
- 1189 Finkelstein, I. J. and Greene, E. C. (2013). Molecular Traffic Jams on DNA. *Annual Review of Biophysics*, 42(1):241–263.
- 1190 Gallagher, L. A., Bailey, J., and Manoil, C. (2020). Ranking essential bacterial processes by speed of mutant death. *Proceedings of the National Academy of Sciences*.
- 1192 Gama-Castro, S., Salgado, H., Santos-Zavaleta, A., Ledezma-Tejeida, D., Muñiz-Rascado, L., García-Sotelo, J. S., Alquicira-Hernández, K., Martínez-Flores, I., Pannier, L., Castro-Mondragón, J. A., Medina-Rivera, A., Solano-Lira, H., Bonavides-Martínez, C., Pérez-Rueda, E., Alquicira-Hernández, S., Porrón-Sotelo, L., López-Fuentes, A., Hernández-Koutoucheva, A., Moral-Chávez, V. D., Rinaldi, F., and Collado-Vides, J. (2016). RegulonDB version 9.0: High-level integration of gene regulation, coexpression, motif clustering and beyond. *Nucleic Acids Research*, 44(D1):D133–D143.
- 1197 Godin, M., Delgado, F. F., Son, S., Grover, W. H., Bryan, A. K., Tzur, A., Jorgensen, P., Payer, K., Grossman, A. D., Kirschner, M. W., and Manalis, S. R. (2010). Using buoyant mass to measure the growth of single cells. *Nature Methods*, 7(5):387–390.
- 1199 Guo, Y., Li, D., Zhang, S., Yang, Y., Liu, J.-J., Wang, X., Liu, C., Milkie, D. E., Moore, R. P., Tulu, U. S., Kiehart, D. P., Hu, J., Lippincott-Schwartz, J., Betzig, E., and Li, D. (2018). Visualizing Intracellular Organelle and Cytoskeletal Interactions at Nanoscale Resolution on Millisecond Timescales. *Cell*, 175(5):1430–1442.e17.
- 1202 Harris, L. K. and Theriot, J. A. (2018). Surface Area to Volume Ratio: A Natural Variable for Bacterial Morphogenesis. *Trends in microbiology*, 26(10):815–832.
- 1204 Hauryliuk, V., Atkinson, G. C., Murakami, K. S., Tenson, T., and Gerdes, K. (2015). Recent functional insights into the role of (p)ppGpp in bacterial physiology. *Nature Reviews Microbiology*, 13(5):298–309.
- 1206 Heldal, M., Norland, S., and Tumyr, O. (1985). X-ray microanalytic method for measurement of dry matter and elemental content of individual bacteria. *Applied and Environmental Microbiology*, 50(5):1251–1257.
- 1208 Henkel, S. G., Beek, A. T., Steinsiek, S., Stagge, S., Bettenbrock, K., de Mattos, M. J. T., Sauter, T., Sawodny, O., and Ederer, M. (2014). Basic Regulatory Principles of *Escherichia coli*'s Electron Transport Chain for Varying Oxygen Conditions. *PLoS ONE*, 9(9):e107640.
- 1211 Hui, S., Silverman, J. M., Chen, S. S., Erickson, D. W., Basan, M., Wang, J., Hwa, T., and Williamson, J. R. (2015). Quantitative proteomic analysis reveals a simple strategy of global resource allocation in bacteria. *Molecular Systems Biology*, 11(2):e784–e784.
- 1214 Ingledew, W. J. and Poole, R. K. (1984). The respiratory chains of *Escherichia coli*. *Microbiological Reviews*, 48(3):222–271.
- 1215 Ireland, W. T., Beeler, S. M., Flores-Bautista, E., Belliveau, N. M., Sweredoski, M. J., Moradian, A., Kinney, J. B., and Phillips, R. (2020). Deciphering the regulatory genome of *Escherichia coli*, one hundred promoters at a time. *bioRxiv*.
- 1217 Jensen, R. B., Wang, S. C., and Shapiro, L. (2001). A moving DNA replication factory in *Caulobacter crescentus*. *The EMBO journal*, 20(17):4952–4963.
- 1219 Jun, S., Si, F., Pugatch, R., and Scott, M. (2018). Fundamental principles in bacterial physiology - history, recent progress, and the future with focus on cell size control: A review. *Reports on Progress in Physics*, 81(5):056601.
- 1221 Karp, P. D., Billington, R., Caspi, R., Fulcher, C. A., Latendresse, M., Kothari, A., Keseler, I. M., Krummenacker, M., Midford, P. E., Ong, Q., Ong, W. K., Paley, S. M., and Subhraveti, P. (2019). The BioCyc collection of microbial genomes and metabolic pathways. *Briefings in Bioinformatics*, 20(4):1085–1093.
- 1224 Karr, J. R., Sanghvi, J. C., Macklin, D. N., Gutschow, M. V., Jacobs, J. M., Bolival, B., Assad-Garcia, N., Glass, J. I., and Covert, M. W. (2012). A Whole-Cell Computational Model Predicts Phenotype from Genotype. *Cell*, 150(2):389–401.
- 1226 Keseler, I. M., Mackie, A., Santos-Zavaleta, A., Billington, R., Bonavides-Martínez, C., Caspi, R., Fulcher, C., Gama-Castro, S., Kothari, A., Krummenacker, M., Latendresse, M., Muñiz-Rascado, L., Ong, Q., Paley, S., Peralta-Gil, M., Subhraveti, P., Velázquez-Ramírez, D. A., Weaver, D., Collado-Vides, J., Paulsen, I., and Karp, P. D. (2017). The EcoCyc database: reflecting new knowledge about *Escherichia coli*K-12. *Nucleic Acids Research*, 45(D1):D543–D550.

- 1230 Khademian, M. and Imlay, J. A. (2017). *Escherichia coli* cytochrome c peroxidase is a respiratory oxidase that enables the use of
1231 hydrogen peroxide as a terminal electron acceptor. *Proceedings of the National Academy of Sciences*, 114(33):E6922–E6931.
- 1232 Klumpp, S. and Hwa, T. (2014). Bacterial growth: Global effects on gene expression, growth feedback and proteome partition.
1233 *Current Opinion in Biotechnology*, 28:96–102.
- 1234 Klumpp, S., Zhang, Z., and Hwa, T. (2009). Growth Rate-Dependent Global Effects on Gene Expression in Bacteria. *Cell*,
1235 139(7):1366–1375.
- 1236 Kostinski, S. and Reuveni, S. (2020). Ribosome Composition Maximizes Cellular Growth Rates in *E. coli*. *Physical Review Letters*,
1237 125(2):028103.
- 1238 Kraemer, J. A., Sanderlin, A. G., and Laub, M. T. (2019). The Stringent Response Inhibits DNA Replication Initiation in *E. coli* by
1239 Modulating Supercoiling of oriC. *mBio*, 10(4):822.
- 1240 Lascu, I. and Gonin, P. (2000). The Catalytic Mechanism of Nucleoside Diphosphate Kinases. *Journal of Bioenergetics and Biomem-
1241 branes*, 32(3):237–246.
- 1242 Laxhuber, K. S., Morrison, M. J., Chure, G., Belliveau, N. M., Strandkvist, C., Naughton, K. L., and Phillips, R. (2020). Theoretical
1243 investigation of a genetic switch for metabolic adaptation. *PLOS ONE*, 15(5):e0226453.
- 1244 Lex, A., Gehlenborg, N., Strobel, H., Vuillemot, R., and Pfister, H. (2014). UpSet: visualization of intersecting sets. *IEEE Transactions
1245 on Visualization and Computer Graphics*, 20(12):1983–1992.
- 1246 Li, G.-W., Burkhardt, D., Gross, C., and Weissman, J. S. (2014). Quantifying absolute protein synthesis rates reveals principles
1247 underlying allocation of cellular resources. *Cell*, 157(3):624–635.
- 1248 Liebermeister, W., Noor, E., Flamholz, A., Davidi, D., Bernhardt, J., and Milo, R. (2014). Visual account of protein investment in
1249 cellular functions. *Proceedings of the National Academy of Sciences*, 111(23):8488–8493.
- 1250 Liu, M., Durfee, T., Cabrera, J. E., Zhao, K., Jin, D. J., and Blattner, F. R. (2005). Global Transcriptional Programs Reveal a Carbon
1251 Source Foraging Strategy by *Escherichia coli*. *Journal of Biological Chemistry*, 280(16):15921–15927.
- 1252 Lu, D., Grayson, P., and Schulten, K. (2003). Glycerol Conductance and Physical Asymmetry of the *Escherichia coli* Glycerol Facili-
1253 tator GlpF. *Biophysical Journal*, 85(5):2977–2987.
- 1254 Lynch, M. and Marinov, G. K. (2015). The bioenergetic costs of a gene. *Proceedings of the National Academy of Sciences*,
1255 112(51):15690–15695.
- 1256 Maaløe, O. (1979). *Regulation of the Protein-Synthesizing Machinery—Ribosomes, tRNA, Factors, and So On*. Gene Expression.
1257 Springer.
- 1258 Metzl-Raz, E., Kafri, M., Yaakov, G., Soifer, I., Gurvich, Y., and Barkai, N. (2017). Principles of cellular resource allocation revealed
1259 by condition-dependent proteome profiling. *eLife*, 6:e03528.
- 1260 Mikucki, J. A., Pearson, A., Johnston, D. T., Turchyn, A. V., Farquhar, J., Schrag, D. P., Anbar, A. D., Priscu, J. C., and Lee, P. A. (2009).
1261 A Contemporary Microbially Maintained Subglacial Ferrous "Ocean". *Science*, 324(5925):397–400.
- 1262 Milo, R., Jorgensen, P., Moran, U., Weber, G., and Springer, M. (2010). BioNumbers—the database of key numbers in molecular
1263 and cell biology. *Nucleic Acids Research*, 38(suppl_1):D750–D753.
- 1264 Monod, J. (1947). The phenomenon of enzymatic adaptation and its bearings on problems of genetics and cellular differentiation.
1265 *Growth Symposium*, 9:223–289.
- 1266 Monod, J. (1949). The Growth of Bacterial Cultures. *Annual Review of Microbiology*, 3(1):371–394.
- 1267 Morgenstein, R. M., Bratton, B. P., Nguyen, J. P., Ouzounov, N., Shaevitz, J. W., and Gitai, Z. (2015). RodZ links MreB to cell wall
1268 synthesis to mediate MreB rotation and robust morphogenesis. *Proceedings of the National Academy of Sciences*, 112(40):12510–
1269 12515.
- 1270 Neidhardt, F. C., Ingraham, J., and Schaechter, M. (1991). *Physiology of the Bacterial Cell - A Molecular Approach*, volume 1. Elsevier.
- 1271 Ojkic, N., Serbanescu, D., and Banerjee, S. (2019). Surface-to-volume scaling and aspect ratio preservation in rod-shaped bacteria.
1272 *eLife*, 8:642.
- 1273 Patrick, M., Dennis, P. P., Ehrenberg, M., and Bremer, H. (2015). Free RNA polymerase in *Escherichia coli*. *Biochimie*, 119:80–91.

- 1274 Peebo, K., Valgepea, K., Maser, A., Nahku, R., Adamberg, K., and Vilu, R. (2015). Proteome reallocation in *Escherichia coli* with
1275 increasing specific growth rate. *Molecular BioSystems*, 11(4):1184–1193.
- 1276 Phillips, R. (2018). Membranes by the Numbers. In *Physics of Biological Membranes*, pages 73–105. Springer, Cham, Cham.
- 1277 Ranganathan, S., Tee, T. W., Chowdhury, A., Zomorodi, A. R., Yoon, J. M., Fu, Y., Shanks, J. V., and Maranas, C. D. (2012). An
1278 integrated computational and experimental study for overproducing fatty acids in *Escherichia coli*. *Metabolic Engineering*,
1279 14(6):687–704.
- 1280 Rogers, H., Perkins, H., and Ward, J. (1980). *Microbial Cell Walls and Membranes*. Chapman and Hall, London.
- 1281 Roller, B. R. K., Stoddard, S. F., and Schmidt, T. M. (2016). Exploiting rRNA operon copy number to investigate bacterial reproduc-
1282 tive strategies. *Nature microbiology*, 1(11):1–7.
- 1283 Rosenberg, H., Gerdes, R. G., and Chegwidden, K. (1977). Two systems for the uptake of phosphate in *Escherichia coli*. *Journal of*
1284 *Bacteriology*, 131(2):505–511.
- 1285 Ruppe, A. and Fox, J. M. (2018). Analysis of Interdependent Kinetic Controls of Fatty Acid Synthases. *ACS Catalysis*, 8(12):11722–
1286 11734.
- 1287 Schaechter, M., Maaløe, O., and Kjeldgaard, N. O. (1958). Dependency on Medium and Temperature of Cell Size and Chemical
1288 Composition during Balanced Growth of *Salmonella typhimurium*. *Microbiology*, 19(3):592–606.
- 1289 Schmidt, A., Kochanowski, K., Vedelaar, S., Ahrné, E., Volkmer, B., Callipo, L., Knoops, K., Bauer, M., Aebersold, R., and Heinemann,
1290 M. (2016). The quantitative and condition-dependent *Escherichia coli* proteome. *Nature Biotechnology*, 34(1):104–110.
- 1291 Scott, M., Gunderson, C. W., Mateescu, E. M., Zhang, Z., and Hwa, T. (2010). Interdependence of cell growth and gene expression:
1292 origins and consequences. *Science*, 330(6007):1099–1102.
- 1293 Shi, H., Bratton, B. P., Gitai, Z., and Huang, K. C. (2018). How to Build a Bacterial Cell: MreB as the Foreman of *E. coli* Construction.
1294 *Cell*, 172(6):1294–1305.
- 1295 Si, F., Le Treut, G., Sauls, J. T., Vadia, S., Levin, P. A., and Jun, S. (2019). Mechanistic Origin of Cell-Size Control and Homeostasis in
1296 Bacteria. *Current Biology*, 29(11):1760–1770.e7.
- 1297 Si, F., Li, D., Cox, S. E., Sauls, J. T., Azizi, O., Sou, C., Schwartz, A. B., Erickstad, M. J., Jun, Y., Li, X., and Jun, S. (2017). Invariance of
1298 Initiation Mass and Predictability of Cell Size in *Escherichia coli*. *Current Biology*, 27(9):1278–1287.
- 1299 Sohlenkamp, C. and Geiger, O. (2016). Bacterial membrane lipids: Diversity in structures and pathways. *FEMS Microbiology*
1300 *Reviews*, 40(1):133–159.
- 1301 Soufi, B., Krug, K., Harst, A., and Macek, B. (2015). Characterization of the *E. coli* proteome and its modifications during growth
1302 and ethanol stress. *Frontiers in Microbiology*, 6:198.
- 1303 Stasi, R., Neves, H. I., and Spira, B. (2019). Phosphate uptake by the phosphonate transport system PhnCDE. *BMC Microbiology*,
1304 19.
- 1305 Stouthamer, A. H. (1973). A theoretical study on the amount of ATP required for synthesis of microbial cell material. *Antonie van*
1306 *Leeuwenhoek*, 39(1):545–565.
- 1307 Stouthamer, A. H. and Bettenhausen, C. W. (1977). A continuous culture study of an ATPase-negative mutant of *Escherichia coli*.
1308 *Archives of Microbiology*, 113(3):185–189.
- 1309 Szenk, M., Dill, K. A., and de Graff, A. M. R. (2017). Why Do Fast-Growing Bacteria Enter Overflow Metabolism? Testing the
1310 Membrane Real Estate Hypothesis. *Cell Systems*, 5(2):95–104.
- 1311 Taheri-Araghi, S., Bradde, S., Sauls, J. T., Hill, N. S., Levin, P. A., Paulsson, J., Vergassola, M., and Jun, S. (2015). Cell-size control
1312 and homeostasis in bacteria. - PubMed - NCBI. *Current Biology*, 25(3):385–391.
- 1313 Taniguchi, Y., Choi, P. J., Li, G.-W., Chen, H., Babu, M., Hearn, J., Emili, A., and Xie, X. S. (2010). Quantifying *E. coli* proteome and
1314 transcriptome with single-molecule sensitivity in single cells. *Science (New York, N.Y.)*, 329(5991):533–538.
- 1315 Tatusov, R. L., Galperin, M. Y., Natale, D. A., and Koonin, E. V. (2000). The COG database: a tool for genome-scale analysis of
1316 protein functions and evolution. *Nucleic Acids Research*, 28(1):33–36.
- 1317 Taymaz-Nikerel, H., Borujeni, A. E., Verheijen, P. J. T., Heijnen, J. J., and van Gulik, W. M. (2010). Genome-derived minimal metabolic
1318 models for *Escherichia coli* mg1655 with estimated in vivo respiratory ATP stoichiometry. *Biotechnology and Bioengineering*,
1319 107(2):369–381. _eprint: <https://onlinelibrary.wiley.com/doi/10.1002/bit.22802>.

- 1320 The Gene Ontology Consortium (2018). The Gene Ontology Resource: 20 years and still GOing strong. *Nucleic Acids Research*,
1321 47(D1):D330–D338.
- 1322 Valgepea, K., Adamberg, K., Seiman, A., and Vilu, R. (2013). *Escherichia coli* achieves faster growth by increasing catalytic and
1323 translation rates of proteins. *Molecular BioSystems*, 9(9):2344.
- 1324 Virtanen, P., Gommers, R., Oliphant, T. E., Haberland, M., Reddy, T., Cournapeau, D., Burovski, E., Peterson, P., Weckesser, W.,
1325 Bright, J., van der Walt, S. J., Brett, M., Wilson, J., Jarrod Millman, K., Mayorov, N., Nelson, A. R. J., Jones, E., Kern, R., Larson,
1326 E., Carey, C., Polat, İ., Feng, Y., Moore, E. W., Vand erPlas, J., Laxalde, D., Perktold, J., Cimrman, R., Henriksen, I., Quintero,
1327 E. A., Harris, C. R., Archibald, A. M., Ribeiro, A. H., Pedregosa, F., van Mulbregt, P., and Contributors, S. . . (2020). SciPy 1.0:
1328 Fundamental Algorithms for Scientific Computing in Python. *Nature Methods*, 17:261–272.
- 1329 Volkmer, B. and Heinemann, M. (2011). Condition-Dependent Cell Volume and Concentration of *Escherichia coli* to Facilitate
1330 Data Conversion for Systems Biology Modeling. *PLOS ONE*, 6(7):e23126.
- 1331 Vollmer, W., Blanot, D., and De Pedro, M. A. (2008). Peptidoglycan structure and architecture. *FEMS Microbiology Reviews*,
1332 32(2):149–167.
- 1333 Weber, J. and Senior, A. E. (2003). ATP synthesis driven by proton transport in F1F0-ATP synthase. *FEBS Letters*, 545(1):61–70.
- 1334 Willsky, G. R., Bennett, R. L., and Malamy, M. H. (1973). Inorganic Phosphate Transport in *Escherichia coli*: Involvement of Two
1335 Genes Which Play a Role in Alkaline Phosphatase Regulation. *Journal of Bacteriology*, 113(2):529–539.
- 1336 You, C., Okano, H., Hui, S., Zhang, Z., Kim, M., Gunderson, C. W., Wang, Y.-P., Lenz, P., Yan, D., and Hwa, T. (2013). Coordination
1337 of bacterial proteome with metabolism by cyclic AMP signalling. *Nature*, 500(7462):301–306.
- 1338 Yu, X., Liu, T., Zhu, F., and Khosla, C. (2011). In vitro reconstitution and steady-state analysis of the fatty acid synthase from
1339 *Escherichia coli*. *Proceedings of the National Academy of Sciences*, 108(46):18643–18648.
- 1340 Zhang, Z., Aboulwafa, M., and Saier, M. H. (2014). Regulation of crp gene expression by the catabolite repressor/activator, cra,
1341 in *Escherichia coli*. *Journal of Molecular Microbiology and Biotechnology*, 24(3):135–141.
- 1342 Zhu, M. and Dai, X. (2019). Growth suppression by altered (p)ppGpp levels results from non-optimal resource allocation in
1343 *Escherichia coli*. *Nucleic Acids Research*, 47(9):4684–4693.

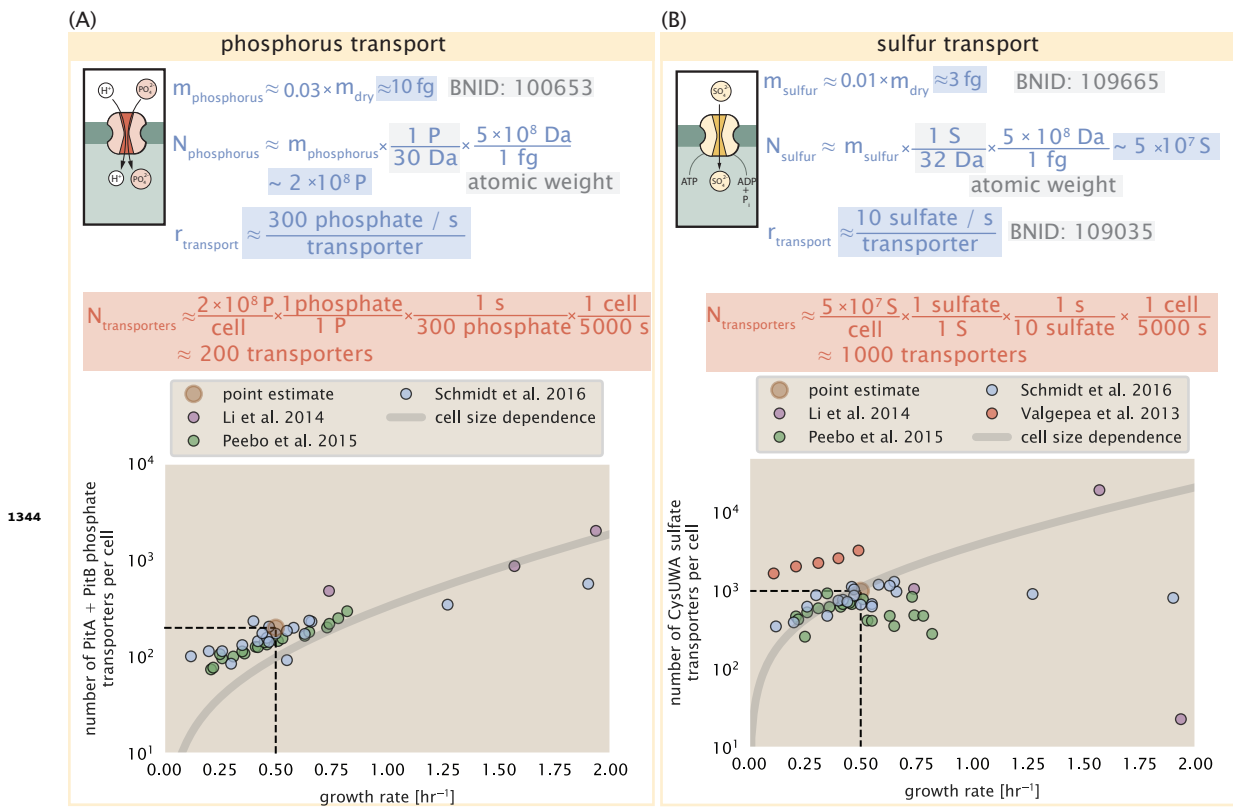


Figure 2-Figure supplement 1. (A) Estimate for the number of PitA phosphate transport systems needed to maintain a 3% phosphorus *E. coli* dry mass. Points in plot correspond to the total number of PitA transporters per cell. (B) Estimate of the number of CysUWA complexes necessary to maintain a 1% sulfur *E. coli* dry mass. Points in plot correspond to average number of CysUWA transporter complexes that can be formed given the transporter stoichiometry [CysA]₂[CysU][CysW][Sbp/CysP]. Grey line in (A) and (B) represents the estimated number of transporters per cell at a continuum of growth rates.

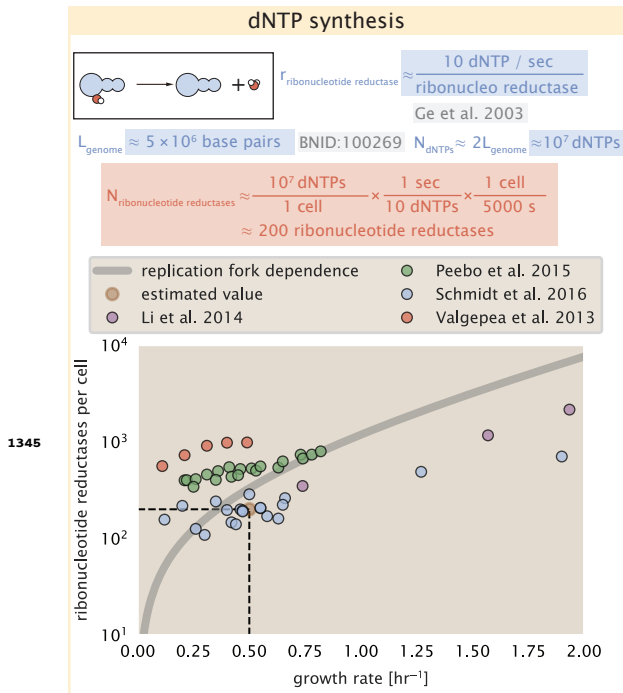


Figure 6–Figure supplement 1. Estimate of the number of ribonucleotide reductase enzymes needed to facilitate the synthesis of $\approx 10^7$ dNTPs over the course of a 5000 second generation time. Points in the plot correspond to the total number of ribonucleotide reductase I ($[\text{NrdA}]_2[\text{NrdB}]_2$) and ribonucleotide reductase II ($[\text{NrdE}]_2[\text{NrdF}]_2$) complexes. Grey lines in top panel show the estimated number of complexes needed as a function of growth, the details of which are described in the Appendix.

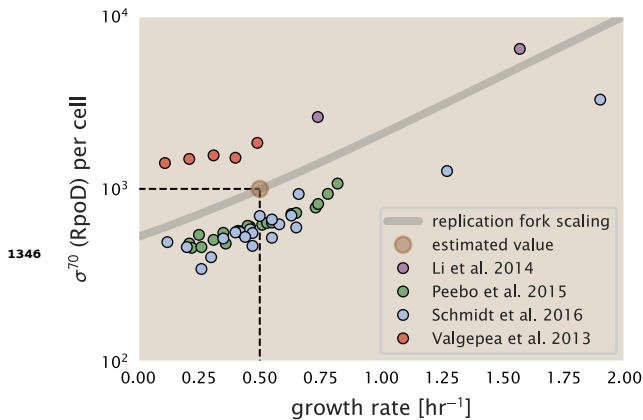


Figure 7–Figure supplement 1. The abundance of σ^{70} as a function of growth rate. Estimated value for the number of RNAP is shown as a translucent brown point and grey line.

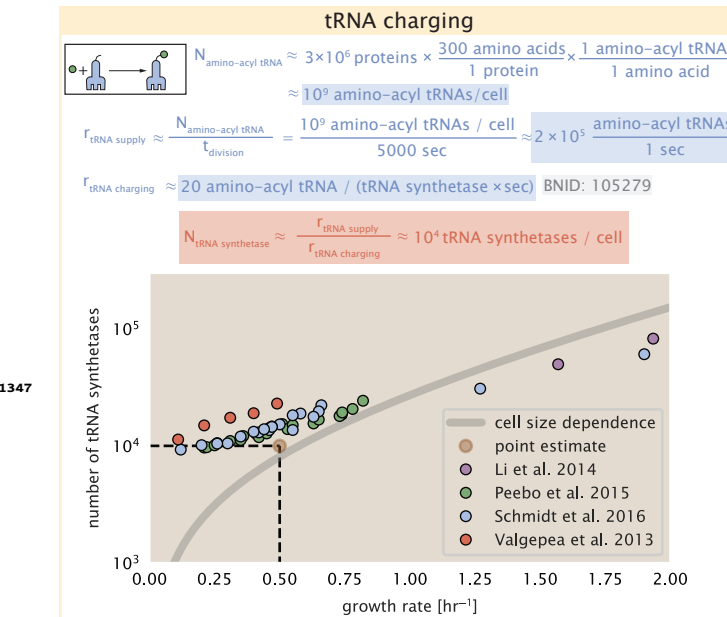


Figure 8-Figure supplement 1. Estimation for the number of tRNA synthetases that will supply the required amino acid demand. The sum of all tRNA synthetases copy numbers are plotted as a function of growth rate ([ArgS], [CysS], [GlnS], [GltX], [IleS], [LeuS], [ValS], [AlaS]₂, [AsnS]₂, [AspS]₂, [TyrS]₂, [TrpS]₂, [ThrS]₂, [SerS]₂, [ProS]₂, [PheS]₂[PheT]₂, [MetG]₂, [lysS]₂, [HisS]₂, [GlyS]₂[GlyQ]₂).

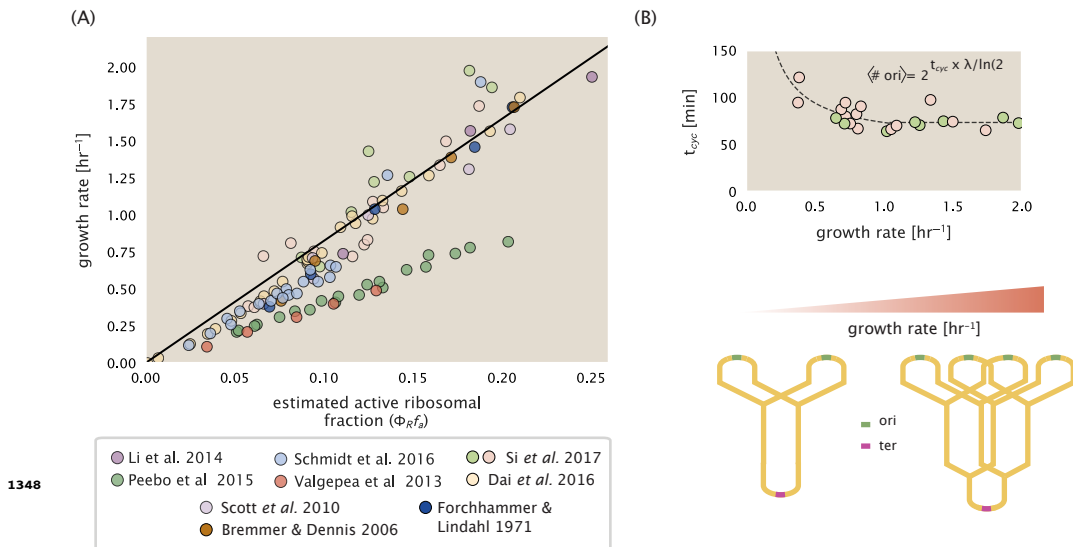


Figure 9-Figure supplement 1. (A) Actively translating ribosomal fraction versus growth rate. The actively translating ribosomal fraction is calculated using the estimated values of f_a from [Dai et al. \(2016\)](#) (shown in inset; see Appendix Calculation of active ribosomal fraction for additional detail). Additional measurements in addition to the proteomic measurements are based on measurements of cellular RNA to protein ratio, with $\Phi_R \approx$ the cellular RNA to protein ratio divided by 2.1 ([Dai et al., 2016](#)). (B) Experimental measurements of the cell doubling time τ and cell cycle time t_{cyc} from [Si et al. \(2017\)](#). Dashed line shows fit to the data, which were used to estimate $\langle \# \text{ori} \rangle$. t_{cyc} was assumed to vary in proportion to τ for doubling times greater than 40 minutes, and reach a minimum value of 73 minutes. See Appendix Estimation of $\langle \# \text{ori} \rangle / \langle \# \text{ter} \rangle$ and $\langle \# \text{ori} \rangle$ for additional details exact estimation of rRNA copy number. Red data points correspond to measurements in strain MG1655, while light green points are for strain NCM3722. Schematic shows the expected increase in replication forks (or number of ori regions) as *E. coli* cells grow faster.